Polar measurements of mesospheric CO
Senior Honors Thesis
Oberlin College Department of Physics and Astronomy

Susannah M. Burrows
susannah.burrows@oberlin.edu

April 18, 2005

Acknowledgements

I wish to thank Professor Christopher Martin for his support, patience, and indomitable enthusiasm throughout this project. He always had a word of encouragement when things seemed most difficult and was available whenever help was needed. Without him, this project could not have happened and I am deeply grateful to him for the opportunities it has afforded me.

I thank all the AST/RO winterovers who collected the data analyzed here: Dr. Wilfred Walsh and Dr. Kechang Xiao (2002); Chris Martin (2001,2003) and Karina Leppik (2003); and Dr. Andrea Löhr and Dr. Stephen Parshley (2005).

I am grateful to AST/RO Principal Investigator Dr. Antony Stark and AST/RO Project Manager Dr. Adair Lane for their advocacy on my behalf. Together with the efforts of Chris and others, their support enabled me to reach Amundsen-Scott South Pole Station and conduct experiments there despite delays and difficulties of many sorts.

Many thanks are also due to Diane Doman for her help in cutting through beaurocratic hurdles and to Lynn Dormand at Raytheon Travel for her concern and help in surviving travel difficulties on two holidays.

Finally, I would like to thank my brother, Daniel Burrows, for his aid and helpful thought on matters of computing; my mother Nancy Burrows and my father David Burrows, for their advice and support; and last but not least, Andreas Werner for his incredible patience and loyalty.

This research was funded in part by grants from the Oberlin College Dean of Arts and Sciences Office and by National Science Foundation grant number ANT-0338150. The AST/RO project is funded by NSF grant ANT-0126090.

Table of Contents

List of Figures

Chapter 1

Introduction

The Earth's atmosphere is an extraordinarily complex dynamical and chemical system, and its behavior can be difficult to predict, as every watcher of televised weather forecasts is aware. Over the past several decades, researchers from a variety of scientific backgrounds have made great advances in our knowledge and understanding of atmospheric systems. The forces driving this research are clear: even the economic, military, and humanitarian implications of our ability to predict everyday weather are more than enough justification. Since the early 1980s, the need for such research has become even more apparent in light of the mounting evidence for human-caused changes in climate patterns that have remained stable for centuries (Houghton & et al. (1996); Houghton et al. (2001)).

However, our ability to model long-term climate change, understand global atmospheric dynamics, or even predict tomorrow's weather is only as good as the data that enters predictive models. The quantity of data needed to describe atmospheric processes can be extremely large, especially as the time scale and geographic scale of the problem increase. Thus, any work in atmospheric science must include three fundamental elements: a theoretical framework, a numerical implementation of that model, and empirical input and verification.

In order to provide some empirical input, we have pursued a study of winds in the Antarctic mesosphere derived from carbon monoxide emission spectra measured at Amundsen-Scott South Pole Station. The observations were made during the years 2002–2005 using the Antarctic Sub-millimeter Telescope / Remote Observatory (AST/RO). The paucity of experimental data describing the Antarctic middle and upper atmosphere has severely hampered climate modelling in this region. Major GCMs (Global Climate Models or Global Circulation Models) either neglect the polar regions completely or reach only to within a few degrees latitude of the Poles. We hope that the results of this study will find application as ground truth to establish the accurate calibration of satellite measurements and as a test of the predictions of GCMs at high latitudes.

The theoretical model used to describe the physics of remote radiometric measurements incorporates elements from quantum mechanics and classical blackbody theory, while any model describing the atmospheric distribution of carbon monoxide must incorporate both photochemistry and circulation models. Although the principal focus of this paper is the reduction of radiometric data, a discussion of aeronomy is also included to place this work in a broader context.

1.1 Spectral Lines of Carbon Monoxide

Carbon monoxide (CO) is a linear, asymmetric diatomic molecule. Like other molecules of this type, it can be modelled as a rigid rotor with quantized angular momentum. A relatively simple analysis shows (*cf.* S2.3.1) that transition energies of a rigid rotor are given by integer multiples of a constant derived from molecular properties. For CO, this constant

is about 115 GHz, the frequency of the $J = 1 \rightarrow 0$ transition, so that the emission frequencies of the CO rotational transitions are given by the simple relation:

$$\nu = J \cdot (115\text{GHz}). \tag{1.1}$$

Equation 1.1 decribes an idealized spectrum of essentially discrete emission frequencies. In reality, it is precisely the deviations from this idealized model that are important, because those deviations result from the relevant physical properties of the system. Most deviations fall under the heading of "spectral broadening," due in atmospheric measurements primarily to collisions with the surrounding atoms and molecules. The resultant spectral line has a typical resonance peak, with line center ν_0 and half-width $\Delta\nu$. When $\Delta\nu \ll \nu$, the shape function near the line center can be approximated by:

$$\gamma = \frac{8\pi^2 N f}{3ckT}|\mu_{ij}|^2\nu^2\frac{\Delta\nu}{(\nu-\nu_0)^2+(\Delta\nu)^2}, \tag{1.2}$$

where c is the speed of light, k is Boltzmann's constant, N is the molecular number density, μ_{ij} is the molecule's magnetic moment (in components), v_0 is the source frequency, and f is the quantum state population ratio (Townes & Schawlow, 1975). The line width is related to the mean time between collisions, τ, by $\Delta\nu = \frac{1}{2\pi\tau}$. Since the rate of molecular collisions is directly proportional to atmospheric pressure, this phenomenon is normally called pressure broadening (*cf.* S2.3.4).

The frequency of the line center, ν_0, depends mainly on the quantum mechanical properties of the molecule in question. But the movement of an entire airmass parallel to the observer's line of sight results in a Doppler shift of the line center by ν_{dopp}. This is modelled by the simple substitution $\nu_0 \longrightarrow \nu_0 + \nu_{dopp}$. After determining ν_{dopp}, we can easily calculate the observed component of wind velocity:

$$v_i = \nu_{dopp}(c/\nu) \tag{1.3}$$

Finally, the pressure of the source region is proportional to $\Delta\nu$.

For simple molecules, a possible approach would be to determine all factors in Equation 1.2 using statistical or other methods. However, in practice this proves quite complex. The unavoidable approximations inherent in such calculations are always specific to the characteristics of the molecule in question, so that there is no model capable of universally predicting these values, even for simpler molecules (Townes & Schawlow, 1975, p. 348). In practice, the coefficients are obtained experimentally. Many are available publically in various databases, which notably include the Jet Propulsion Laboratory (JPL) Spectral Line Catalog (Pickett et al., 1998), used in this work.

Before the radiation emitted by mesospheric carbon monoxide reaches the surface and is measured, it must pass through the Earth's lower atmosphere. The model must therefore also take into account any loss due to radiative transfer. The greatest effect on mesospheric emission spectra is absorption by the broad spectral bands of O_2 and H_2O in the troposphere. This effect is frequency-dependent, but we will consider it to be constant over our observation bandwidth. Various methods are available to estimate the atmospheric opacity (*cf* S3.6).

The so-called forward model incorporates all the relevant aspects of theory and experimental design to give a full mathematical description of the experimental set-up. As far is possible and reasonable, it includes known instrumental parameters, such as antenna efficiency and receiver noise. Once the forward model is complete, inverse modelling methods can be applied to estimate the atmospheric state based on the observed spectra, as described in Chapter 4.

1.2 Radiometry

Radiometry has been used to observe atmospheric parameters since the 1950s. Much study has been devoted to determining the concentrations of photochemically significant atmospheric components such as H_2O and O_3. In particular, many of the pioneering studies of the Antarctic ozone hole used radiofrequency emission spectra to show the strong seasonal and latitudinal variations in O_3 concentrations. Radiometry has several distinct advantages as an experimental method. First, radiometric measurement can serve as a data source that, unlike bal-

loon or rocket measurements, is near-continuous in time. Close to the poles, not even satellites make continuous observations, since geostationary satellites cannot measure these regions and polar satellites provide only intermittant data. Also unlike many satellite measurements, radiometric observations often have vertical structure, and can yield vertical profiles of variables such as molecular concentration and temperature. A radio telescope observes the entire atmosphere along its line-of-sight simultaneously, and can collect information difficult to access using other techniques. In particular, the region of the atmosphere providing the strongest carbon monoxide emission signal, between about 40 km and 80 km in altitude, is difficult to measure using balloons, satellites, or other methods. Balloon measurements at the South Pole provide vertical profiles until measurements stop due to mechanical failure in the increasingly cold environment, typically at about 30 km altitude. Meteor radars and measurements of the aurora by optical telescopes have been used in studies of the thermosphere, but these phenomena do not occur significantly below about 80 km (Hernandez et al. (1996); Forbes et al. (1999); Portnyagin et al. (2000); Portnyagin et al. (1997); Marsh et al. (2000)).

Once deemed docile and unimportant, the upper atmospheric regions became the subject of so much research by the mid-20th century that a new term, "Aeronomy," was coined in 1953 to describe their study (Fukushima, 1995). The mesospheric region, difficult to measure with most remote sensing techniques, is of particular interest due to its role as a boundary between the neutral lower atmosphere and the highly charged upper atmosphere. Measuring atmospheric dynamics from the earth's rotational pole is especially interesting. Previous studies have shown that certain global wind patterns do not appear in the polar regions (Hernandez et al., 1995; Hernandez, 1999).

The first intentional measurements of atmospheric carbon monoxide were made in 1975 by Waters et al. (1976). Since that time, CO has been recognized as an important tracer of the dynamics of the middle and upper atmosphere. Because of its long photochemical lifetime (on the order of about a month), mesospheric carbon monoxide has a density profile that is heavily dependent on the details of atmospheric transport processes. However, the number of published studies remains surprisingly small compared to studies of other atmospheric species. For a review of the history of mesospheric CO observations, see de Zafra & Muscari (2004). In the past, most continuous measurements of atmospheric CO have been obtained by mid-latitude ground observations of the $J = 1 \rightarrow 0$ transition and more recently, by satellite measurements (one exception is Wattenbach et al. (1984), in which the 691-GHz J=6←5 transition was observed). AST/RO is capable of observing the $J = 2 \rightarrow 1$, $J = 4 \rightarrow 3$, and $J = 7 \rightarrow 6$ rotational transitions of CO at a broad range of altitudes in the upper mesosphere and lower thermosphere, between about 40 and 130 km. First results using this technique by Chamberlin (1997) have already produced preliminary mesospheric wind velocity data and density and mixing profile results.

Chapter 2

Theory

To understand the emission spectra considered in this study, it is neccessary to have a working model of the radiation source. This model must include some assumptions about the distribution and physical state of the source molecules and their environment.

2.1 Structure of the Earth's Atmosphere

Atmospheric scientists divide the Earth's atmosphere into a set of layers with boundaries defined by the atmosphere's temperature profile. As a result, the altitudes at which these layers occur are not fixed but vary in time and with location. In fact, the temporal and geographic changes in the atmosphere's vertical structure are an active subject of research. Typically, four layers are distiguished. The lowest layer of the atmosphere is the troposphere, reaching up to an altitude of about 10 km (Chamberlin, 2001). It is characterised by a rapid decrease in temperature with altitude, which ends at the tropopause, the troposphere's upper boundary. The stratosphere lies between about 12 and 40–50 km altitude and is characterised by a constant or increasing temperture profile. The mesosphere is the region between about 40-50 km and 80-90 km in altitude, in which the temperature again drops off, reaching its lowest point at the mesosphere's upper boundary, the mesopause. Above the mesopause lies the highly ionized thermosphere, which acts as a dumping ground for solar energy. Among the photochemical cycles that prevail only at these high altitudes is the photolytic reaction chain that produces mesospheric CO. The temperature structure of the atmosphere is very well-researched at mid-latitudes and reference models such as the US Standard Atmosphere (1976) are quite reliable for these regions. However, the temperature structure of the Antarctic mesosphere was not carefully measured until recent decades (Lübken et al. (1999), Hernandez et al. (1992), Pan & Gardner (2003)). As an approximation, the predictions of the MSISE Model 1990 model (Figures 2.1 and 2.2) are useful. The MSISE-90 model provides predictions for neutral temperature, density, and the concentrations of several atmospheric components as a function of geographic location and time. Its predictions reach up to 1000 km in altitude. In the lower and middle atmosphere, the model is largely based on the MAP handbook (Labitzke et al., 1985). Above 72.5 km, the MSISE-90 is essentially a revision of the 1986 Mass-Spectrometer-Incoherent-Scatter (MSIS) model (Hedin, 1987). The MSISE-90 and other standard atmospheric models are obtainable from the National Space Science Data Center website [1].

2.2 Aeronomy of CO

In 1954, Sidney Chapman coined the term "Aeronomy" to categorize "the science of the upper atmospheric regions where dissociation and ionization are

[1] *http://nssdc.gsfc.nasa.gov/space/model/atmos/atmos_index.html*

important." (qtd. in Fukushima (1995)). The study of aeronomy has been characterized as "The branch of science dealing with the atmosphere of the Earth and the other planets with reference to their chemical composition, physical properties, relative motion, and reactions to radiation from outer space." (Chambers dictionary of science and technology, cited in Brasseur & Solomon (1984), p. ix).

Research in the field of aeronomy has been fueled since the early 1980s by the discovery of the Antarctic ozone "hole" and the subsequent investigation of ozone chemistry. Trace gases and aerosols that do not play a crucial role in ozone photochemical cycle have received little attention. One molecule that has been neglected by aeronomy is carbon monoxide. Since the first measurement by Waters et al. (1976), only a handful of papers have been published on mesospheric CO. However, as noted in the introduction, carbon monoxide can play a significant role in improving our understanding of atmospheric dynamics and deserves scientific attention in its role as a tracer (de Zafra & Muscari, 2004).

The concentrations of atmospheric components is typically described in terms of the molar mixing ratio, the relative concentration of a particular component with respect to all atmospheric molecules. The mixing ratio of carbon monoxide is determined by two very different production processes in the upper and lower atmosphere, which compete with rapid CO destruction in the stratosphere to produce a complex distribution. Figure 2.3 provides an overview of mid-latitude vertical profile measurements through 1986, while Figure 2.4 shows the polar profile retrieved by Chamberlin (1997) using AST/RO data. The peak in the absolute volume density of carbon monoxide near 50 km in altitude represents the portion of this spectrum that can be best observed radiometrically. This section gives an overview of the major processes that determine the vertical distribution of carbon monoxide in the atmosphere.

Carbon monoxide occurs naturally in the troposphere in concentrations up to about 10^{-7}ppm, primarily as an oxidation product of biologically produced methane. But between about 20 km and 60 km in altitude, CO is rapidly oxidized by the hydroxyl radical ($OH\cdot$):

$$CO + OH\cdot \longrightarrow CO_2 + H\cdot \tag{1}$$

The comparatively high concentrations of $OH\cdot$in the middle and upper atmosphere are the result of photodissociation of $H_2O$by incoming solar radiation. The rate at which carbon monoxide is destroyed depends on the frequency of collisions between $OH\cdot$and CO molecules. Very little tropospheric CO survives the rapid destruction by $OH\cdot$in the relatively dense troposphere, causing the mixing ratio of CO to decline to a minimum near 20 km.

As the altitude increases, the atmosphere rapidly becomes "thinner," i.e. there is a decrease both in volume number density and in pressure. As the atmospheres thins, molecules spread out and collisions occur less frequently. The destruction of carbon monoxide by Reaction 1 slows and above 20 km the CO mixing ratio rises again. The source of this mesospheric carbon monoxide is downwelling from the thermosphere, where CO is produced by photolysis:

$$CO_2 + h\nu \longrightarrow CO + O \tag{2}$$

Photolytic production is rapid only at high altitudes, where incoming solar radiation at the relevant wavelengths has not yet been attenuated by the absorption bands of atmospheric O_2. Reaction 2 dominates the CO budget in the upper mesospheric and lower thermosphic regions. Above about 100km, CO is again destroyed, primarily through recombination with atomic oxygen in the presence of a third body (Solomon et al., 1985):

$$CO + O + M \longrightarrow CO_2 + M. \tag{3}$$

Although the mixing ratio of CO continues to climb for altitudes up to about 100 km, absolute concentrations reach a maximum between 50 and 60 km in altitude. As a result, most submillimeter emission by CO comes from an altitude range between about 50 and 90 km above the earth's surface, resulting in a very narrow spectral line (*cf* SS2.3.4).

In the absence of sunlight, the photochemical reactions described above clearly cannot take place. Consequently, one would expect to observe high seasonal fluctuations in the carbon monoxide column density

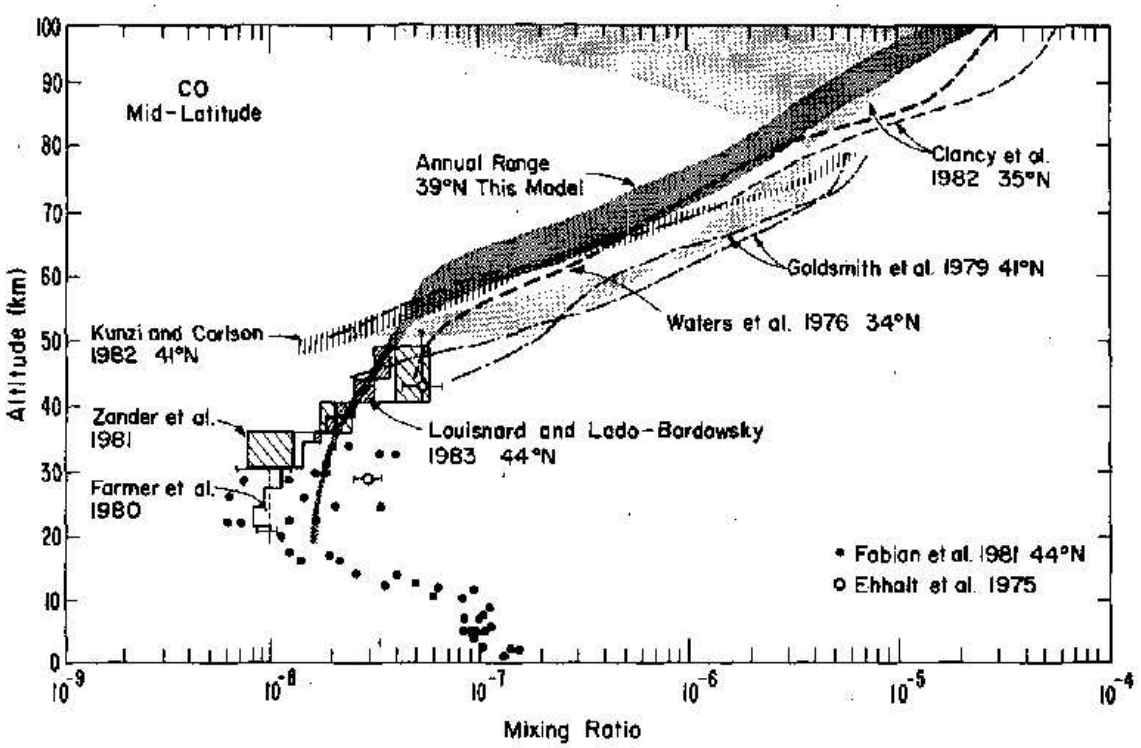

Figure 2.3: Predicted and measured carbon monoxide profiles through 1985, as presented in Solomon et al. (1985). The dark shaded region shows the annual range prediction from that study, while the light shaded region shows an uncertainty estimate for microwave mesospheric observation (Clancy et al., 1982). Stratospheric measurements were taken by infrared and cryogenic sampling methods.

corresponding to the seasonal variations in insolation. Prior to 1985, one-dimensional models predicted that CO concentrations would reach a maximum in summer, when both photochemical production and destruction processes are at a maximum. However, experimental results showed the opposite effect (Clancy et al., 1982). The authors correctly concluded that the answer to this mystery lay in the sensitivity of the carbon monoxide distribution to atmospheric transport processes.

In the early 1980s, Rudolph Garcia and Susan Solomon developed a two-dimensional atmospheric model which incorporated the major dynamical and chemical processes in the middle atmosphere, spanning from pole to pole and from about 16 to 116 km in altitude (Garcia & Solomon, 1983). Using this new model, Garcia and Solomon showed the photochemical lifetime of CO in the mesosphere to be comparable to the time scales of both vertical eddy diffusion and advection.

In the 1985 paper by Solomon et al., still the definitive analyis of mesospheric carbon monoxide concentrations, the seasonal variation in the CO column density is explained, and predictions are made about its geographic distribution. According to the model, decreased photochemical production of CO in the winter months is more than compensated by meridional transport from the summer hemisphere to the winter hemisphere and also by winter downwelling from the thermospheric source region. Since there is decreased destruction by Reaction 1 (on page 5) during the winter months, the CO concentration can increase dramatically. The paper also included a prediction of unusually high CO concentrations in the polar winter atmosphere, due to the virtual absence of recombinatory processes. At the time, there were no high-latitude CO observations available to test this prediction. At mid-latitudes, the column density of mesospheric CO in winter has been shown to be roughly twice the summer value (Clancy et al., 1982).

In 1991-1992, the Improved Stratospheric and Mesospheric Sounder (ISAMS) on the Upper Atmospheric Research Satellite (UARS) collected data on high-latitude CO distributions. Analysis of these observations (de Zafra & Muscari (2004), Allen et al. (1999), Allen et al. (2000)) has supported the prediction of high polar concentrations.

Most recently, de Zafra & Muscari (2004) made high-latitude measurements of the $J = 2 \rightarrow 1$ transition of CO at Thule, Greenland (76°N). The measurements were made in the winters of 2002 and 2003, and were compared to trial observations made at the South Pole during the austral summer of 1999-2000. Evidence was found for a large pole-to-pole gradient, as predicted by Solomon et al. (1985).

Calculations by Chamberlin (1997) based on AST/RO data show that the mesospheric CO near the South Pole is primarily concentrated between about 50 km and 60 km in altitude (see Figure 2.4). In this region, the temperature predictions of the MSIS model range between 281 and 290 K in January and between 251 and 275 K in the winter.

2.3 Physics of emission spectra

2.3.1 The Rigid Rotor

The rotational spectrum of an isolated assymetric diatomic molecule can be modelled by considering the molecule to be a rigid rotor; that is, two nuclei spearated by a fixed distance flipping end-over-end about the center of mass. Using this model, the energy transitions can be obtained rather simply. Following Townes & Schawlow (1975) (Ed. 1, p. 3), we first use Bohr's assumption of angular momentum quantized in units of $h/2\pi$. From Newtonian physics, we obtain

$$2\pi f I = \frac{Jh}{2\pi} \tag{2.1}$$

where I is the molecular moment of inertia about axes perpendicular to the internuclear axis, and J is the angular momentum "quantum number." The frequency of the emitted light is equal to the frequency f of molecular rotation. We neglect rotation about the internuclear axis since the moment of inertia about this axis is a few thousand times smaller, producing emissions with frequencies lying near the visible range (Townes & Schawlow, 1975, ed. 1, p. 3).

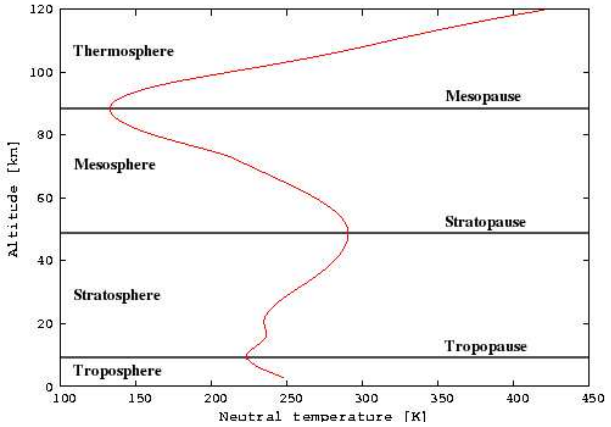

Figure 2.1: Temperature stucture and layers of the atmosphere. Atmospheric temperature profile from the MSISE-90 model for 90°S on January 1, 2004 at 0h UT.

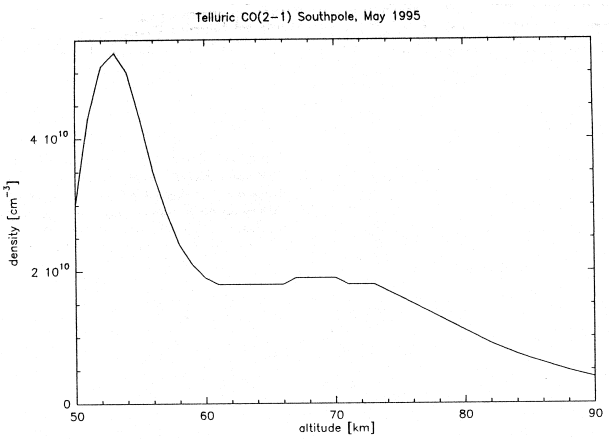

Figure 2.4: Density-altitude profile of CO measured by AST/RO at South Pole, (Chamberlin, 1997).

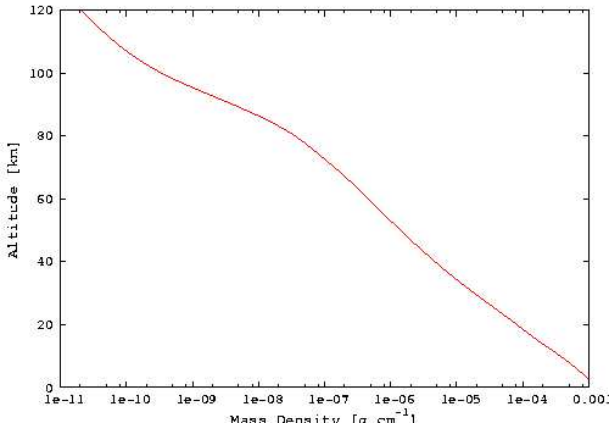

Figure 2.2: Vertical mass density profile from the MSISE-90 model for 90°S on January 1, 2004 at 0h UT.

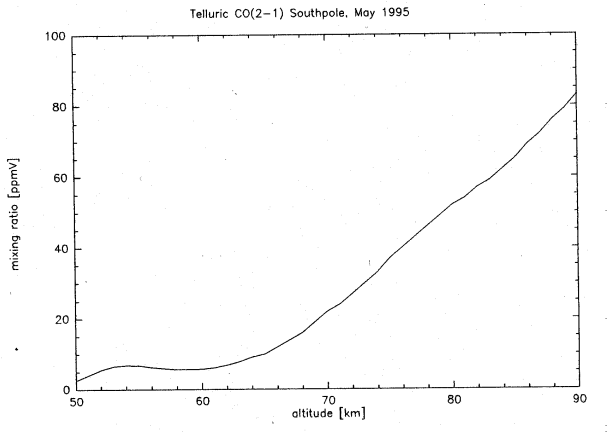

Figure 2.5: Vertical CO mixing ratio profile measured by AST/RO at South Pole, (Chamberlin, 1997).

2.3.2 Factors Affecting Line Shape

A simplistic understanding of basic quantum mechanics may seem to suggest that molecular emission and absorption of radiation should occur at discrete energies, i.e. that the spectral lines have a width of zero. In fact, a certain finite width is necessary as a result of the zero-point electromagnetic vibrations. At low temperatures, the vibrational energy due to zero-point fields is $h\nu$, but at ordinary temperatures, thermal radiation becomes most significant, with a mean energy of kT for each mode of vibration of the field. At room temperature, the absorption line has a half width at half maximum intensity of about 4×10^{-5} Hz (Townes & Schawlow, 1975, p. 336).

However, experiment shows that spectral lines have significant width and a common typical shape, which depend on parameters such at atmospheric pressure, wind speed, and molecular properties. Modern theory has produced a number of competing mathematical models which approximate the shapes of these lines various well under varous conditions. An excellent reference work and starting point for understanding microwave spectra is the classic work by Townes & Schawlow (1975).

2.3.3 Doppler Broadening and Line Center Shift

Random kinetic motion of molecules also leads to a broadening of lines due to the Doppler effect. The process by which this broadening occurs is fairly straightforward. A molecule is moving with velocity v parallel to an observer's line of sight and emits radiation which has a frequency ν_0 in the molecular reference frame. As is well known, the signal measured by the observer is then shifted in frequency from the line center by $\nu_{\rm dopp} = \nu_0(v/c)$. In order to determine the Doppler broadening, we must take into account the distribution of velocities within the atmosphere at a particular temperature T. Boltzmann statistics shows the the probability of a molecule in a gas having a velocity v in a particular direction is proportional to

$$\exp\left(\frac{-mv^2}{2kT}\right) = \exp\left[\left(\frac{-mc^2}{2kT}\right)\left(\frac{\epsilon}{\nu_0}\right)^2\right]. \quad (2.2)$$

This is in turn proportional to the line intensity as a function of the distance from line center, ϵ. The Doppler line shape is:

$$D(\nu,\nu_0) = \frac{(\ln 2/\pi)^{1/2} e^{-\ln 2((\nu-\nu_0)/\Delta\nu_d)^2}}{\Delta\nu_d} \quad (2.3)$$

where $\Delta\nu_d$ is the line's half-width at half maximum:

$$\Delta\nu_d = \frac{\nu_0}{c}\sqrt{\frac{2kT}{m}\ln 2} = 3.581 \times 10^{-7}\sqrt{\frac{T}{M}}\nu_0. \quad (2.4)$$

where M is the molecular weight (*cf* Janssen, 1993, p. 339; Townes & Schawlow, 1975, p. 337). For the $J = 2 \rightarrow 1$ transition of carbon monoxide (with a molecular weight of 28 amu) at $T = 250$K, the Doppler width is $\Delta\nu = 2.5 \times 10^4$ Hz. As we will see, this effect is somewhat less than the pressure broadening of mesospheric CO emission lines, which is about 3.5×10^4 Hz. At present, our fitting algorithm accounts only for pressure broadening, described below, and does not include the broadening of lines due to thermal effects.

For bodies of air with net motion along the line of sight, the line center itself is shifted, providing a mechanism for remote measurement of atmospheric winds. We assume the observed mesospheric wind has uniform horizontal velocity v_x directed away from the telescope and vertical velocity v_y upwards. At a given telescope elevation, the shift of the line center is given by

$$\nu_{\rm dopp} = -\left[\frac{v_x}{c}\cos\theta + \frac{v_y}{c}\sin\theta\right] + \nu_\delta. \quad (2.5)$$

The constant ν_δ is a frequency offset due to possible calibration errors. In order to correct for ν_δ and reduce the measurement solely to horizontal wind speed, a second determination of $\nu_{\rm dopp}$ is made in the opposite azimuthal direction. By subtracting the Doppler shift in the second spectrum, $\nu_{\rm dopp,2}$ from

that in the first spectrum, $\nu_{\mathrm{dopp},1}$, we obtain

$$\nu_{\mathrm{dopp},2} - \nu_{\mathrm{dopp},1} = \frac{2v\cos\theta}{c}\nu_0, \tag{2.6}$$

$$v = \frac{c}{2\cos\theta}\frac{\nu_{\mathrm{dopp},2} - \nu_{\mathrm{dopp},1}}{\nu_0}. \tag{2.7}$$

The resolution of our wind speed determinations is proportional to the relative uncertainty in the fit to the parameter ν_{dopp}:

$$\frac{\sigma_v}{v} = \frac{c}{2\cos(\theta)}\frac{1}{\nu_0}\left[\frac{\sigma_{\nu_{dopp,1}}}{\nu_{dopp,1}} + \frac{\sigma_{\nu_{dopp,2}}}{\nu_{dopp,2}}\right], \tag{2.8}$$

with uncertainties σ_v and $\sigma_{\nu_{\mathrm{dopp}}}$ in the velocity and retrieved Doppler shift. A frequency shift of 32 kHz, one full channel of our AOS spectrometer, corresponds to a change in wind speed of 42 m/s. However, we achieve significantly better resolution by utilising the full peak in fitting, as decribed in Chapter 4.

It should be noted that this calculation assumes the winds to be essentially constant throughout a large geographical area. At 15° elevation, measurements of a CO layer at 50 km altitude are actually sensing a region located 187 km distant geographically. Moreover, the telescope azimuth determines the time zone and thereby the local time of the region being measured. In fact, because of the unique location of the South Pole, any local time can be observed simply by rotating the remote sensing instrument, a fact that can be exploited to study the longitudinal progression of atmospheric waves (Hernandez et al., 1995).

2.3.4 Pressure Broadening

A theoretical model describing the emission spectra of collision-broadened lines was developed in 1945 by van Vleck and Weisskopf (van Vleck & Weisskopf, 1945). By re-examining the underlying conceptual model of molecular interactions, they showed the two previously dominant theories to be special cases of a more generalized expression for the line shape, characterised by a line width parameter $\Delta\nu$ and a resonant frequency ν_0.

One early theory, developed by Debye, considered only "nonresonant" absorption, which lacks a characteristic absorption peak. In the Debye absorption model, a fixed dipole with no rotational or translational energy undergoes a collision. After the collision, the dipole is assumed to be preferentially oriented with respect to the electric field. The liklihood of a particular orientation is by the Boltzmann distribution $\exp(-\mathbf{E}\cdot\mu/kT)$, ensuring statistical equilibrium. During this orientation process, the molecule absorbs a small amount of energy. Van Vleck and Weisskopf recognized that Debye's model is in fact a special case of $\nu_0 = 0$ within a general theory of resonant and non-resonant absorption. As such, it is a good approximation for spectra with $\nu_0 \ll \Delta\nu$.

In contrast, Lorentz' theory assumed that molecules are randomly aligned after a collision. This assumption quietly glosses over the tendency of the molecular dipole moments to align with the ambient electric field. As a result, the Lorentz model is accurate only when statistical broadening effects are small compared to the resonant frequency, $\Delta\nu \ll \nu_0$.

The advantage of the new theory developed by van Vleck and Weisskopf was its applicability regardless of the size of the ratio ν_0/ν. In particular, it became possible to quantitatively understand emission spectra in the microwave region, where the inequality $\Delta\nu/\nu \ll 1$ is often unsatisfied and the Lorentz model is not applicable.

It is also important to note the physical significance of the factor $\Delta\nu$. Van Vleck and Weisskopf used the definition $\Delta\nu = \frac{1}{2\pi\tau}$, where τ is the mean time between collisions. A simple analysis shows that the atmospheric pressure p is inversely proportional to τ, so $p \propto \Delta\nu$. Equation 1.2, repeated here for convenience, approximates the absorption coefficient γ of a collision-broadened spectral line in the region near the line center:

$$\gamma = \frac{8\pi^2 N f}{3ckT}|\mu_{ij}|^2\nu^2\frac{\Delta\nu}{(\nu-\nu_0)^2 + (\Delta\nu)^2}. \tag{2.9}$$

The constant c is the speed of light, k is Boltzmann's constant, N is the molecular number density, μ_{ij} is the molecule's electric dipole moment (by components), v_0 is the source emission frequency, $\Delta\nu$ is the

line width factor and f is the quantum state population ratio (Townes & Schawlow, 1975).

Both the state ratio f and the line width factor are functions of T. The ratio of occupied states f is governed by the Boltzmann statistical distribution. The collisional line width is generally given in terms of a set of collision parameters (Janssen, 1993, p. 340):

$$\Delta\nu = \Delta\nu_0(P/P_0)(T/T_0)^{-x}. \tag{2.10}$$

The overall temperature dependence of the van Vleck-Weisskopf line shape is approximately $T^{-\lambda}$, for some factor λ determined by the properties of the molecule and its environment. Since $x \approx 1$ for much of the microwave region, the spectral intensity is relatively insensitive to uncertainties or errors in T,a particularly attractive feature of the microwave region.

2.3.5 Other measures of spectral lines

It is sometimes of interest to have a measure of the total amount of CO in the atmosphere without vertical resolution that can be easily compared between observing locations and seasons. One such metric is the column density, defined as the local mass or number density of an atmospheric component per unit area of the earth's surface,

$$\int_0^\infty \rho(z)dz \tag{2.11}$$

where $\rho(z)$ is the density as a function of height.

Another constant is the integrated line intensity, defined in Townes & Schawlow (1975, p. 343, ed. 1) as

$$\int_0^\infty \frac{\gamma}{\nu^2}d\nu \tag{2.12}$$

Its advantage lies in the fact that the value is independent of pressure broadening. In Townes & Schawlow (1975, p. 344, ed. 1) it is shown that

$$\int_0^\infty \frac{\gamma}{\nu^2}d\nu = \frac{8\pi^3 Nf}{3ckt}\left|\mu_i j\right|^2, \tag{2.13}$$

which is independent of $\Delta\nu$.

Chapter 3

Data collection: experimental design and observation techniques

3.1 AST/RO telescope

The Antarctic Submillimeter Telescope and Remote Observatory (AST/RO) is a 1.7 m diameter heterodyne telescope located at the US National Science Foundation (NSF) Amundsen-Scott South Pole Station (Stark et al., 2001). It was installed during the 1995-6 austral season and has been used primarily for astronomical research. More information on the telescope and related research programs can be found on the AST/RO website[1].

3.2 AST/RO instrument characteristics

The AST/RO telescope currently includes eight heterodyne receivers and an imaging Fabry-Perot interferometer (SPIFI), sensitive to a variety of frequency ranges. Of chief interest for this paper is the 230 GHz niobium-aluminum-niobium SIS (superconductor-insulator-superconductor) double-sideband receiver, known as "Major Dobbins," made in 1989 at Bell Laboratories by J. Bally. SIS Josephson junction mixers achieve very low receiver noise in the frequency range above about 50 GHz. However, because the critical temperature of niobium is 7 K, the receiver requires liquid helium cryogenics during operation. A second SIS receiver, called "Wanda," is capable of observing at 460 and 806 GHz.

spectively.

In every observation scan, two acousto-optical spectrometers (AOSs) were used: a low resolution spectrometer (LRS) with 1 GHz bandwidth (bandpass 1.6 – 2.6 GHz) and a high resolution spectrometer (HRS) with 60 MHz bandwidth (bandpass 60 – 120 MHz) (Schieder et al., 1989). The LRS has a pixel spacing of 670 kHz with 1.1 MHz resolution bandwidth per pixel. For the HRS, the pixel spacing is 32 kHz with 60 kHz resolution bandwidth. After any alterations or repairs to the AOS, this pixel spacing is recalibrated. The telescope is also equipped for precise optical pointing and tracking of astronomical objects (the optical system of the telescope is depicted in Figure 3.2). However, the details of optical pointing and spatial resolution are unimportant for the purpose of atmospheric measurements. For a technical description of the optical and mechanical design of the AST/RO telescope, see Stark et al. (1997).

AST/RO observes CO lines on a regular basis during astronomical data collection as part of the automatic re-calibration and sky noise estimation. Each sky scan typically represents only a few seconds of observing time. However, the winter mesospheric CO spectral line is strong enough to be clearly visible on these sky scans, providing a near-continuous source of atmospheric CO observations. CO has a very simple emission spectrum, as discussed elsewhere (*cf* S 2.3.1).

[1] *http://cfa-www.harvard.edu/~adair/AST"˙RO/*

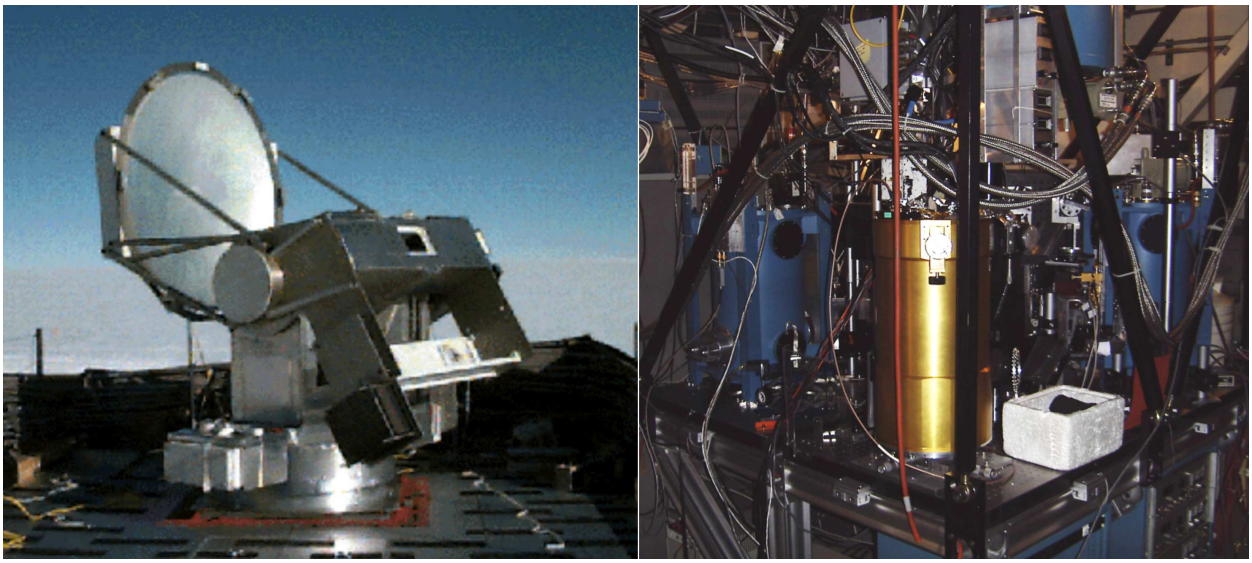

Figure 3.1: Left: The AST/RO telescope dish. The dish is capable of pointing between about 12° and 75° above the horizon. During repairs, the area around the telescope can be protected from the weather using the canvas-covered structure visible in the background. During storms with high winds, the telescope can be "parked" pointing upwards to reduce the risk of wind damage to the dish, which can act like a sail under windy conditions. Photo courtesy of the Center for Astrophysical Research in Antarctica, online Virtual Tour of Submillimeter Experiments at *http://astro.uchicago.edu/cara/vtour/pole/darksector/submm/* Right: The AST/RO optics table, with cryostatic dewars. The table is located directly below the telescope dish, inside a heated room.

The lines available to us are the J=2→1, J=4→3, and J=7→6 rotational transitions of carbon monoxide, at 230.6, 461, and 806 GHz, re

3.3 Site Characteristics

The AST/RO instrument is located at the NSF Amundsen-Scott South Pole Station, at about 89° 50′ south latitude and 45° 53′ west longitude. Its location in the so-called "Dark Sector" places it far enough from the station to minimize interference from communications equipment and other noise sources. The telescope is staffed each year by two "winter-overs," who arrive during the austral spring and spend a full year at the South Pole. In the summer, teams of scientists come to the station in small groups to install and maintain equipment, carry out observations, etc.

It is well known that astronomical observations can best be made at high-altitude, dry sites, where there is minimal absorption of radiation from astronomical sources by the atmosphere. Similarly, in atmospheric studies, emitted radiation from higher parts of the atmosphere can be heavily attenuated by tropospheric water vapor and oxygen. At an elevation of 2,847 m (9,341 ft) above sea level, the surface air pressure is lowered even further by the permanent polar low covering the polar regions. In 2002 and 2003, the average barometric pressures at the surface were 680.5 hPa and 681.3 hPa, respectively, and ranged from 656.2 hPa to 708.0 hPa, averaging 680.5 hPa and 681.3 hPa, respectively (Climate Monitoring and Diagnostics Laboratory (CMDL), 2004). This implies

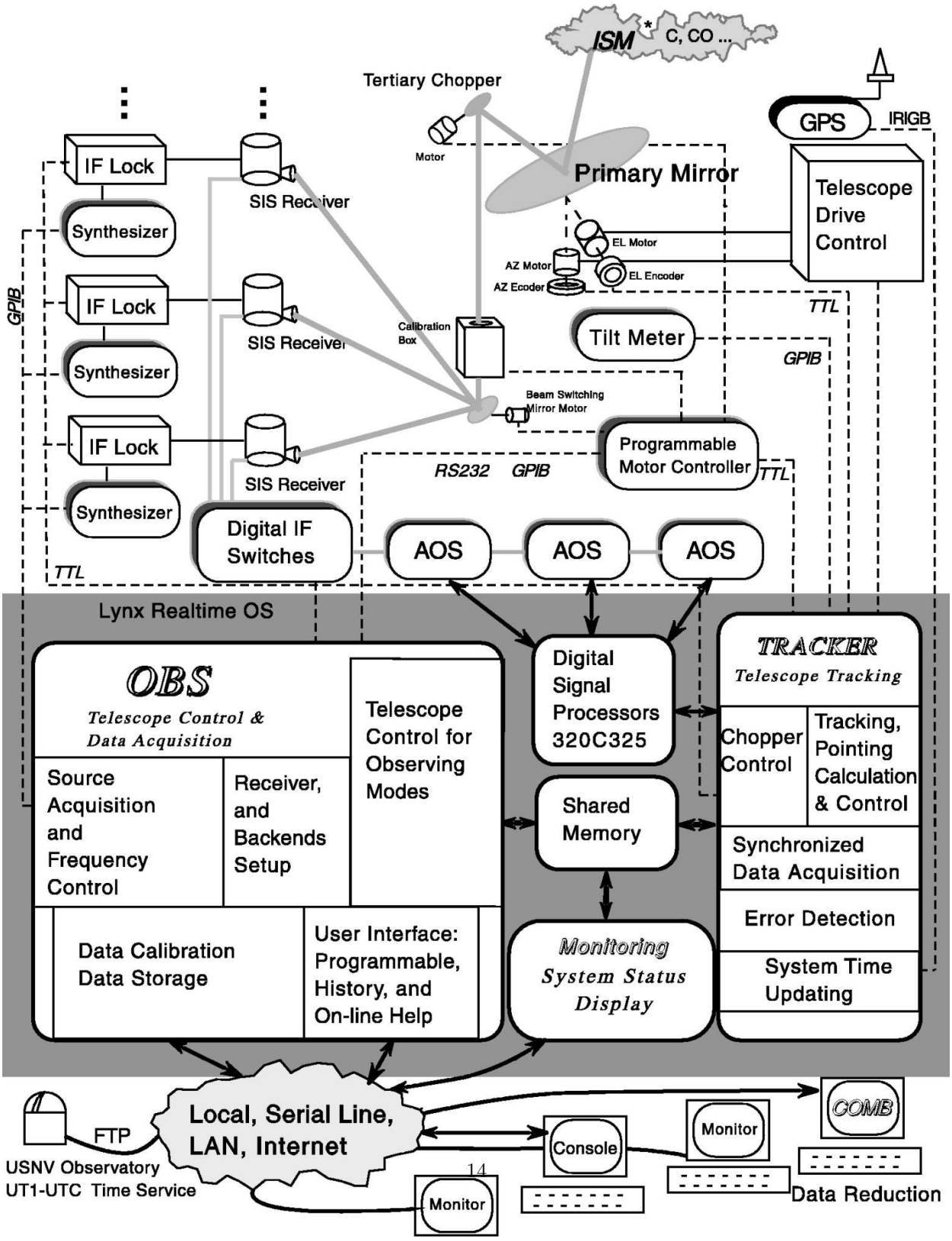

Figure 3.4: Block diagram of AST/RO control system. The region in the gray box represents the telescope control and data processing computer (Stark et al., 2001).

that the telescope lies above roughly one-third of the earth's atmosphere. Because of its extreme dryness, the opacity of the atmosphere above the South Pole is lower than any other site in the submillimeter range. The Antarctic plateau is the driest desert on earth, with yearly precipitation at South Pole Station totalling less than 1 mm each year. The average precipitable water vapor in the atmosphere lies below .7 mm on most days of the year, plummeting below .5 mm for the entirety of the winter (*cf.* Figure 3.5). In most locations, water vapor presents the major obstacle to observations in the submillimeter range because of its broad spectral absorption bands at these wavelengths.

3.3.1 Atmospheric Opacity

The optical depth or opacity of the atmosphere is defined by:

$$\tau = \int_0^s \alpha(s')ds', \tag{3.1}$$

where $\alpha(s)$ the absorption coefficient at distance s from the observer along the line of sight.

The atmospheric opacity at the South Pole has been characterized in several studies, including Chamberlin & Bally (1994), Chamberlin (2004), and Chamberlin et al. (1997).

In Chamberlin (2001) and Chamberlin (2002), a high correlation was shown to exist between surface temperature and the precipitable water vapor column (PWV), which is closely related to the atmospheric opacity. Because these studies were all conducted with astronomical research in mind, they give only an overall indication of the atmospheric opacity, with no vertical resolution.

One common method of estimating the tropospheric attenuation is the "skydip" technique (Chamberlain et al., 2000; Chamberlin et al., 1997). In this technique, the antenna temperature is measured at a sequence of different elevation angles. With knowledge of the form of radiative transfer as a function of μ (*cf* S3.4.2), the constant τ_{TROP} can be retrieved by fitting an equation roughly of the form of Equation 3.13 to the data.

An additional source of data quantifying the atmospheric opacity is a 350 micron "tipper" located on the roof of the AST/RO building. Up-to-date opacitymeasurements at that wavelength are available over the internet.[2]

A final source of information on atmospheric opacity is the South Pole meteorology department. The department keeps a record of all major meteorological and climatological variables. In particular, surface temperatures have been logged since the original South Pole station was built in 1957. These surface temperatures can be used to estimate the temperature of the atmosphere when considered as a single blackbody radiator. For 1995, the relation

$$T_{\rm atm}[{\rm K}] = 0.31 T_{\rm sur} + 162 \tag{3.2}$$

was found to represent 90% of the data to within ± 4 K (Ingalls (1999), cited in Stark et al. (2001)).

[2] *http://adelie.harvard.edu/spole/tipper/*

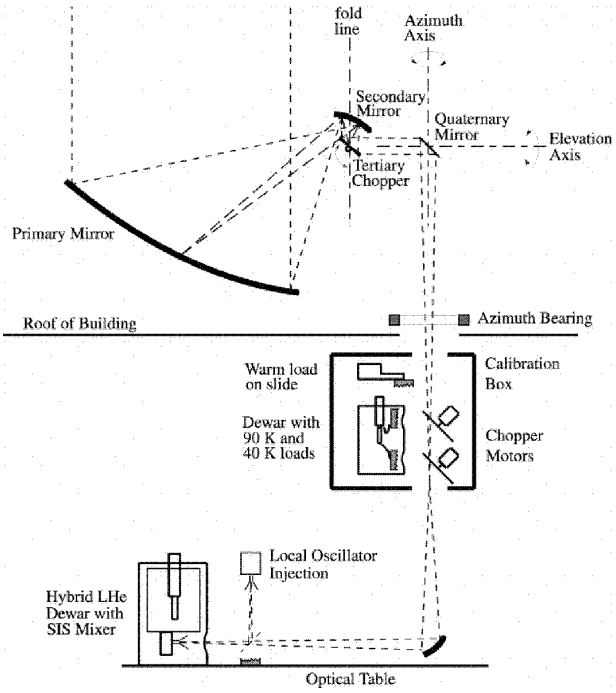

Figure 3.2: Schematic of the AST/RO optical system. The beam path has been flattened by a rotation of 90°about the vertical "fold line." Stark et al. (2001)

Figure 3.3: Susannah Burrows in front of the AST/RO building, January 2005. The telescope dish is mounted on top of the building. Inside is a warm instrument room (see Figure 3.1), storage space, and laboratory space for scientists working on the telescope.

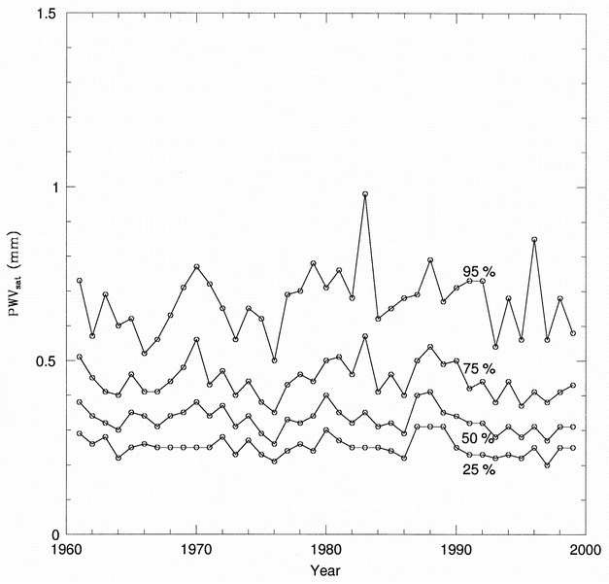

Figure 3.5: Cumulative distribution by year of the precipitable water vapor at saturation (PWVsat) for the winter period, days 100 to 300. The values of the water vapor column density were calculated based on radiosonde temperature measurements with the assumption that the atmosphere was in equilibrium over ice. The lines on this graph show the distribution of PWVsat by percentile, i.e. in each year, 25% of the values of PWVsat fell below the first solid line, 50% below the sencond line, 75% below the third line and 95% below the uppermost solid line (Chamberlin, 2001).

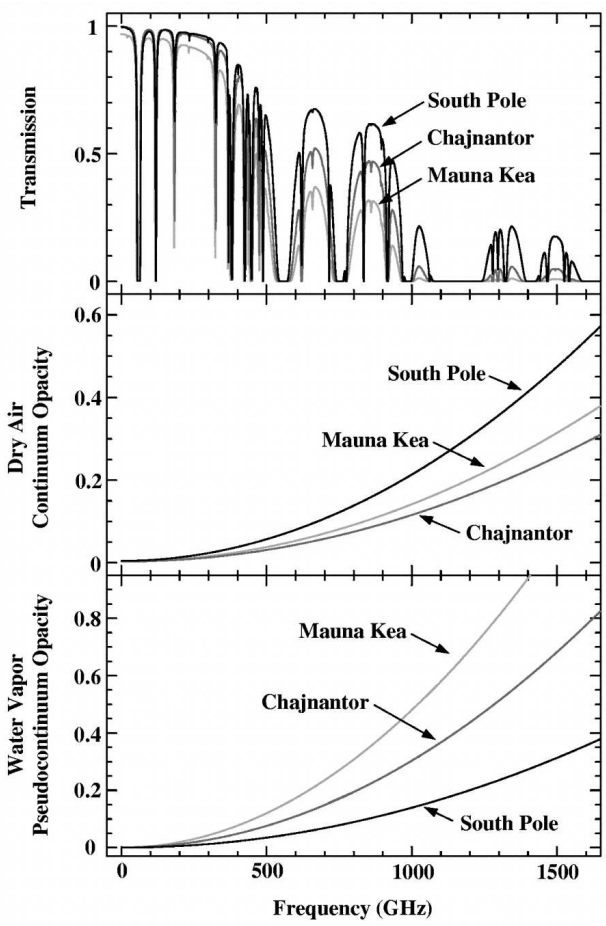

Figure 3.6: Submillimeter tranmittance at three observing locations. The upper plot shows a comparison of the winter atmospheric transmissivity at zenith, calculated by J. R. Pardo using the ATM model (Pardo et al., 2001). Calculations are based on the 25th percentile PWV values at each site (0.2 mm for the South Pole, 0.6 mm for Chajnantor, and 0.9 mm for Mauna Kea). The differences are highly frequency-dependent, and at lower frequencies the Chajnantor curve converges with the South Pole curve. The calculated values of the dry air continuum opacity and the water vapor pseudocontinuum opacity shown in the middle and bottom plots give an indication of the contribution to the opacity of water vapor compared with the dry air component. Of the three sites, opacity is dominated by the dry air component only at the South Pole. Figure from Stark et al. (2001).

3.4 Microwave Radiometry: Theory and Definitions

3.4.1 Equivalent Temperatures

An explanation of telescope calibration first requires a careful mathematical definition of terms used, especially the term "temperature," as it is applied throughout microwave astronomy in a sense very different from, but distantly related to its common thermal definition. Where applicable and unless otherwise noted, this paper follows the definitions suggested in Committee on Earth Observation Satellites (CEOS) (2003), part of an as yet uncompleted project to compile a list of standard definitions used in microwave radiometry.

"Temperatures" in radiometry typically refer to "radiation temperatures," or "equivalent temperatures." Their definitions are closely tied to the thermodynamical theory of blackbody radiation, which establishes a relationship between the physical temperature of a perfect blackbody radiatior and its emitted spectrum. The Planck distribution formula for a blackbody radiator is given by

$$L(\nu,T)d\nu = \frac{2h}{c^2}\left(\frac{\nu^3}{e^{h\nu/kT}-1}\right)d\nu, \tag{3.3}$$

where h is Planck's constant, c is the speed of light, k is Boltzmann's constant, T is the physical temperature of the radiator and $L(\nu,T)d\nu$ is the radiance (sometimes called "brightness"), the radiated power per unit solid angle. It is convenient to define the spectral radiance density, L_f as the radiance per unit frequency interval, $L_f \equiv \frac{dL}{df}$. Over small frequency intervals $d\nu$ (such as the spectrometer bins), L and L_f are approximately constant and we can approximate

$$\int_{\nu}^{\nu+d\nu} L(\nu',T)d\nu' = L_f(\nu,T)\times d\nu \tag{3.4}$$

For low-frequency radiation, this expression can be simplified using the Rayleigh-Jeans approximation, $hv \ll kT$. In this limit, we can make the approximation

$$e^{h\nu/kT} \approx 1 + \frac{h\nu}{kT} + ..., \tag{3.5}$$

which in combination with Equation 3.3 gives the Rayleigh-Jeans law:

$$L_f(\nu,T) \approx \frac{2\nu^2}{c^2}kT. \tag{3.6}$$

The approximation is reasonable for the region of interest, although it becomes progressively worse at higher frequencies. For instance, at T =290 K, $h\nu/kT = 0.0381$ and $e^{h\nu/kT} - 1 = 0.0388$, with a deviation of under 2%. For radiation at 460 GHz, this error climbs to about 3.6%.

Many of the objects observed in radiometry behave like black bodies, to some approximation. However, even the radiation of sources that do not conform to the blackbody model can be quantified in terms of this straightforward theory. For unpolarized radiation, the brightness temperature T_b represents the temperature of a blackbody that would emit the same radiance in the specified frequency interval, obtained in the Rayleigh-Jeans limit by inverting Equation 3.6:

$$T_b(\nu) \equiv \frac{c^2}{2kT\nu^2} \tag{3.7}$$

A fine distinction is made between the antenna temperature T_a and the brightness temperature T_b. An antenna is not a perfect measuring device. Its measurement pattern is anisotropic by design, because spatial resolution is so crucial for astronomical measurements. The antenna temperature is the equivalent of the incoming brightness temperature averaged by the Antenna Directivity $D(\Omega)$. Some input power is converted to heat and this ohmic loss is subsequently re-emitted at the antenna's physical temperature T_p:

$$\begin{aligned} T_a(\Omega_0) &= [\tau/4\pi]\int D(\Omega-\Omega_0)T_b(\Omega)d\Omega \\ &\quad +(1-\tau)T_p \end{aligned} \tag{3.8}$$

in the Rayleigh-Jeans approximation, where τ is the transmission coefficient of the loss element. This deviation is corrected for in the process of telescope calibration (cf 3.5.1).

3.4.2 Radiative Transfer

The signal observed by the telescope is emitted in the mesosphere and must first pass through the highly

absorbant troposphere before being observed. If the troposphere is assumed to have a homogenous opacity $\tau_{\rm TROP}$, tropospheric absorption attenuates the signal by $e^{-\tau_{\rm TROP}/\mu}$. The modifier $\mu = sin(\theta)$ accounts for the different path-lengths through the troposphere dependant on the elevation angle, θ. The air mass through which the observation is taken, normalized to the air mass at 90°, is given by $1/\mu$. The troposphere also emits at these wavelengths, so that the total transfer equation is approximated (for $\tau_{\rm TROP}/\mu \ll 1$) by:

$$T_b^*(\nu) = T_b(\nu)e^{-\tau_{\rm TROP}/\mu} + (1 - e^{-\tau_{\rm TROP}/\mu})T_{\rm TROP}. \tag{3.9}$$

$T_{\rm TROP}$ is the physical temperature of the troposphere and $\tau_{\rm TROP}$ is the sum of the O_2 and H_2O opacities, which can also be measured by various methods (*cf.* S3.6). This quantity is assumed to be constant across the bandwidth, a reasonable assumption because of the high pressure broadening within the troposphere.

3.5 Observation techniques

3.5.1 Gain and frequency calibration

The output signal of the telescope depends not only on the brightness of the source, but also on the receiver response and interference from other emitting and absorbing particles in the atmosphere. By carefully calibrating the instrument, we can convert the measured antenna temperature into the brightness temperature of the source.

In order to determine the receiver response to temperature, the telescope beam is directed to hot and cold loads of known temperatures. Two methods of calibration were used. After each receiver tuning, a manual calibration was undertaken. During observation, periodic automated recalibrations were conducted using the reference loads. The telescope includes three blackbody loads at known physical temperatures: a "hot" load at receiver room ambient temperature, and "cool" load at 90 K, and a "cold" load at 40 K. The cool and cold loads are chilled by a closed cycle refrigerator, but their surfaces are warmed by infrared radiation entering the dewar, so that their effective radiation temperatures are about 100 K and 140 K, respectively. The hot load is mounted on a slider for insertion into the telescope beam. The beam can be redirected to either of the cold loads via a rotating mirror (Stark et al., 2001, p. 580).

In each calibration scan, three measurements are made of the data output of the jth AOS channel, I_j, output by the AOS to the computer in arbitrary intensity units. First, the "zero" measurement ($I_{{\rm zero},j}$) is recorded, which measures the receiver response in the absence of an incoming IF signal. Next, the beam is directed to the calibration loads, and the receiver responses $I_{C,j}$ and $I_{H,j}$ to the cold ($T_B = T_C$) and warm ($T_B = T_W$) loads are recorded by the data acquisition computer. Because the AOS output data values I_j are directly proportional to the incoming power spectrum, any data value can now be easily converted into the equivalent antenna temperature. This is done simply by measuring the proportionality between the output of the AOS and the for each channel:

$$G_j \equiv \frac{I_{W,j} - I_{C,j}}{T_W - T_C}. \tag{3.10}$$

The receiver noise temperature, $T_{\rm rx}$, is a measure of the average level of noise contributed by the receiver, IF system, and AOS. It is defined in Committee on Earth Observation Satellites (CEOS) (2003) as"the input termination noise temperature which, when the input termination is connected to a noise-free equivalent of the receiver, would result in the same output noise power as that of the actual receiver connected to a noise-free input termination." The receiver noise was recalculated during each calibration run. The calibration spectrum is a measure of the noise in each AOS channel:

$$T_{{\rm rx},j} = \frac{I_{C,j} - I_{{\rm zero},j}}{G} - T_C^* \tag{3.11}$$

and the average receiver noise temperature is the average receiver noise temperature:

$$T_{\rm rx} = \frac{1}{N_C}\sum_{j=1}^{N_C} T_{{\rm rx},j} \tag{3.12}$$

(Stark et al. (2001), p. 580). The value of $T_{\rm rx}$ gives a qualitative measure of the quality of a particular data set.

The manual recalibration measures the effective radiation temperatures of the two loads by comparing the receiver response to that of the warm load and a radio-frequency blackbody absorber soaked in liquid nitrogen. In tuning the telescope, both the observed frequency range and the power level of the receiver are changed, which can result in significant changes in receiver response. Consequently, a manual calibration was performed after each new tuning.

In summary, the power spectrum response I_j of the uncalibrated system to an input signal $J_\nu(T)$ is:

$$\begin{aligned} I_j - I_{{\rm zero},j} = \\ G_j\,[\,(T_{b,j} + T_C)e^{-\tau_{\rm TROP}/\mu} \\ + (1 - e^{-\tau_{\rm TROP}/\mu})T_{\rm TROP} + T_{{\rm rx},j}]. \end{aligned} \tag{3.13}$$

The term T_C, included here for generality, is a background blackbody source emitting at essentially constant intensity across the bandwidth. In absorption line studies, this could be the sun or the moon. In emission studies, it is usually the cosmic microwave background, with a temperature of about 3 K.

3.5.2 Frequency Switching

Another method we employed was frequency switching, which results in a measure of self-calibration for receiver noise and background radiation (such as the cosmic microwave background, although its magnitude is negligible for our purposes.) In frequency switching, the receiver alternates between ν_1 and ν_2, two local oscillator (LO) frequencies near the target frequency, which has the effect of shifting the received sectrum. The difference $\nu_{FS} = \nu_1 - \nu_2$ is the frequency switch. The intensity as a function of the distance from the LO at each of the two settings is then differenced. The result is the removal of much of the baseline due to receiver noise or background radiation (for example, from broad O_2 and H_2Oor the cosmic microwave background).

For convenience, we can write the discretely valued quantities I_j, G_j and $T_{{\rm rx},j}$ as continuous functions of ν. For small values of ν_{FS}, we can make the approximation $G(\nu_1) \approx G(\nu_2) \approx G(\overline{\nu})$, where $\overline{\nu}$ is the average of ν_1 and ν_2. Similarly, $T_{\rm rx}(\nu_1) \approx T_{\rm rx}(\nu_2) \approx T_{\rm rx}(\overline{\nu})$ is a reasonable approximation for a "well-behaved" receiver. We can then write the intensity of a frequency-switched emission spectrum as

$$\frac{I(\nu_1) - I(\nu_2)}{G(\overline{\nu})} = [T_{b,j}(\nu_1) - T_{b,j}(\nu_2)]\, e^{-\tau_{\rm TROP}/\mu}. \tag{3.14}$$

Any background radiation T_C is eliminated from this expression, as is the tropospheric emission $(1 - e^{-\tau_{\rm TROP}/\mu})T_{\rm TROP}$. We typically chose values of ν_{FS} ranging between about 8 MHz and 16 MHz. For frequency switches with values of ν_{FS} much greater than these, the approximations $G(\nu) =$ constant and $T_{\rm rx}(\nu) =$ constant are likely to fail. This technical and practical barrier typically limits the application of frequency switching to comparatively narrow spectral lines.

Chapter 4

Data reduction

4.1 Short users guide for MATLAB routines

Each spectrum was fitted using MATLAB's `lsqcurvefit` routine from the Optimization Toolbox, which employs an implementation Levenberg-Marquadt fitting algorithm. The algorithm is a least-squares method first suggested by Levenberg in 1944, which was further developed and implemented in 1963 by Marquardt. It uses an adjustable parameter to transition smoothly between a Newton-Gauss fitting procedure, which is efficient near a local minimum, and the method of steepest descent, which is efficient at locations distant from the local minimum. By combining the advantages of these two mechanisms, the local least-squares solution can be reached efficiently for a wide range of starting conditions.

The bulk of this project involved the development of a set of MATLAB routines to process the CO emission spectra obtained from the AST/RO telescope using `lsqcurvefit`. This section is a brief guide to the routines used, which should prove useful to future students continuing work on the project. The set of routines can be adopted with only minor modifications for use with spectra that may have a different form, by simply writing a new routine containing the form function that replaces `vvwfo`. The full code of the MATLAB routines can be found in Appendix .

Fitting a set of data is a process that involves several steps:

1. *Importing and selecting spectra (cf 4.1.1)*: The user compiles a list of the FITS files in the working directory which will be fitted. A selection process may choose only the subset of spectra which have a particular group of characteristics.

2. *Preprocessing (cf 4.1.2)*: Each spectrum is "folded" as described below. The beginning and ending points of the region to be fitted are determined for each spectrum and stored for further use. An initial guess is obtained for the background function.

3. *Least-squares fitting (cf 4.1.3)*: The routine `timeseries.fo` fits each spectrum to the target function and outputs both the results of the fitting and several other relevant parameters into a set of MATLAB structures.

4. *Post-processing (cf 4.1.4)*: Files flagged in step 3 as having been poorly fitted are reviewed to determine the cause of the failure. Spectral files that are corrupted by telescope noise are identified, and remaining spectra are fitted by repeating steps 2 and 3.

4.1.1 Importing FITS files to MATLAB

Data from the AST/RO telescope are initially processed on-site by the telescope control and data acquisition software "OBS" (see Figure 3.4). The "OBS" software was originally developed for use at Bell Laboratories, and was later modified for use on AST/RO (Huang, 2001). The data files produced by OBS can

be read and processed by the "COMB" data reduction software. In addition to displaying data and performing fits to simple Gaussian and Lorentzian distribution, COMB is capable of quickly searching through large data sets and of exporting data to a more portable format. The exported spectra are saved in the Flexible Image Transport System (FITS) data format, which can be easily read by MATLAB and many other scientific data processing applications.

MATLAB contains two built-in functions, `fitsinfo` and `fitsdata`, for reading the headers and data of FITS files. Because the output generated by these built-ins is unwieldy, the data was imported using a routine called `rfits`, written by A. Bolatto and modified for use in this project. This routine outputs both the relevant header information and the image data to named fields of a single MATLAB structure. A second routine, `foldspectrum`, uses `rfits` to read in a FITS file, then "folds" the data (*cf* S4.1.2) about its switching frequency and outputs the results to a new field in the data structure.

The first step in processing any set of FITS files is to generate a list of data files selected for fitting. Typically, the user will wish to process a subset of files from a large directory that meet a particular group of criteria. A straightforward method of accomplishing this is to first obtain a list of all the filenames in the directory, then narrow that list down to contain only those spectra that are of interest. The built-in command `dir` outputs information about the contents of a target directory into a MATLAB structure. One field of this structure is a cell of strings containing the names of all files in the target directory.

Having obtained a list of file names, the user may wish, for instance, to select only those spectra which were obtained at a particular telescope elevation, tuning frequency, or azimuthal angle. Additionally, spectra with unreasonably large telescope noise, as estimated in the T_{RMS} header, can be discarded (We rejected all data with $T_{rms} > 1000$ with no further processing). This sorting is accomplished via the routine `filter_filevec`.

Once the vector or cell of file names has been constructed, these files can be browsed in MATLAB. The routine `view` makes it possible to quickly view any spectrum in the list graphically. Each spectrum is accessed by inputting the number of the element in the input vector containing its file name. In order to ease viewing, the plot is centered on the expected emission frequency, and the antenna temperature is centered on zero. If the spectrum has already been fitted, `view` can superimpose the best-fit function over the plotted data. For convenience, the most important header variables are printed to the plot, as seen in Figure 4.1. `view` is also useful for excising bad spectra from a list of filenames by hand. The command 'd' deletes the displayed spectrum from a list of names and optionally records the file names of removed spectra in both a MATLAB vector and a `.mat` data file.

4.1.2 Preprocessing

The preprocessing of the data involves three steps. Each spectrum is first "folded" about the line center, then "trimmed" to include only the area near the peaks. Finally, an initial guess is made at the background fit. These three steps are accomplished using the routine `trimauto`, which accepts as input the MATLAB cell `filevec` containing the list of file names.

The "folding" of the spectra helps to reduce underlying background terms. The folding process involves inverting the spectrum, shifting it by an amount equal to the switching frequency, and then adding the transformed spectrum to the orginal. This results in a large central positive peak flanked by two smaller negative peaks, as illustrated in Figures 4.2 and 4.3. It is implemented in the function `foldspectrum`. This function outputs an `rfits` structure with three additional fields. The fields `frequency` and `frequencyfo` contain the frequency vectors (ν) for the unfolded and folded spectra, respectively. The folded data is stored in the field `datafo`.

The telescope's bandwidth is much wider than the observed peaks. As a result, a large portion of the information in a spectrum is not only irrelevant, but may also contain extraneous or misleading information that inteferes with the fitting procedure. For example, the wings of neaby oxygen lines, while relatively constant across the peak, may result in a

greater background near the edges of the bandwidth. Also, the signal-to-noise ratio is best best near the observed line center and worst towards the edges of the spectrometer. Finally, many spectra contained a background ripple, which did not always have a simple form across the full bandpass.

In order to improve the conditions for fitting, each spectrum was "trimmed" to the region between an initial data point n_i and a final point n_f. These points were chosen to correspond to a frequency range of 50 MHz about the line center ν_0.

To determine an initial guess for the background of each spectrum, the background function was fitted to a subset of the data. This subset extended from m_i to n_f but excluded the regions near the peaks, which were assumed to have a width of 20 MHz. The background function used for fitting had the form:

$$B(\nu) = b_1 + b_2 \cdot \nu + b_3 \cdot sin(b_4 \cdot \nu + b_5), \qquad (4.1)$$

where $b_1 ... b_5$ are the elements of the background vector **b**. `trimauto` outputs three MATLAB vectors containing the values of n_i, n_f, and **b** for each spectrum in `filevec`.

4.1.3 Least-squares fitting

Least-squares fitting of a data set is performed by the routine `timeseriesfo`, which then outputs important information into MATLAB structures which can be easily processed further. The format of the structures output by `timeseriesfo` is summarized in Table 4.1.

`timeseriesfo` calls the algorithm `lsqcurvefit` from the MATLAB Optimization Toolbox. `lsqcurvefit` is a front-end for both Gauss-Newton and Levenberg-Marquardt fitting algorithms. As input, it takes the experimental data, a function to be fitted, an initial guess for the parameters, lower and upper bounds on the parameters (not used in the Levenberg-Marquardt routine) and a vector containing the settings of various options. The function being fitted is supplied by `vvwfo`, which also optionally outputs the Jacobian matrix.

The spectra were fitted to a set of 8 parameters, which included a 'magnitude' A, the line width $\Delta\nu$, the Doppler shift $\nu_{\rm dopp}$ and a set of 4 parameters accounting for background "ripples" in the measurements. The emission frequency ν_0 and the telescope elevation factor $\mu = sin(\theta)$ were obtained from information contained in the FITS headers and could be fixed to the correct value for each spectrum. The source function to be fitted was:

$$T_A(\nu) = A\mu\nu^2 \frac{\Delta\nu}{(\nu - \nu_{\rm dopp} - \nu_0)^2 - (\Delta\nu)^2}. \qquad (4.2)$$

Because of the frequency switching technique used, the shape of the line becomes

$$T_{fs}(\nu) = T_A(\nu) - T_A(\nu - \nu_{FS}), \qquad (4.3)$$

where ν_{fs} is the magnitude of the frequency shift, calculated for each spectrum from information stored in the FITS headers.

Least-squares fitting algorithms perform poorly when the parameters to be retrieved are of radically different orders of magnitude. In order to improve the conditions for fitting, the data was scaled and centered by the transformations:

$$\nu' = \nu/\sigma_\nu^2 \qquad (4.4)$$

$$T_A' = (T_A - \mu_{T_A})/\sigma_{T_A}, \qquad (4.5)$$

with μ_{T_A} the mean value of T_A and σ_ν, σ_{T_A}, respectively, the standard deviations in the range of measured frequencies ν and experimental values of T_A. Corresponding calculations "scaled" the state vector before fitting and "unscaled" it after fitting. This scaling step is critical to the satisfactory functioning of the fitting routine.

In calling `timeseriesfo`, the user supplies an initial guess at the parameters $\Delta\nu$, $\nu_{\rm dopp}$ and A as elements of a vector $\mathbf{a_0}$. The routine combines **b** and $\mathbf{a_0}$ to create the state vector $\mathbf{a} = \{a_{0,1}, a_{0,2}, a_{0,3}, b_1, b_2, b_3, b_4, b_5\}$.

Three output structures contain the fitted coefficients and relevant information about the files for 1) successfully fitted spectra, 2) spectra for which the residuals after fitting were large, and 3) spectra for which fitting resulted in a low residual, but an anomalous wind speed (more than three standard deviations from the mean).

An additional routine, `series_excise`, is used to separate a "series" structure containing the fields created by `timeseriesfo` into two separate matlab structures. A logical flag vector is used to select which data should be removed from the original structure. The elements of the flag vector corresponding to data marked for excision are set to 1 (logical true) and all others must be set to zero.

4.1.4 Post-Processing

Once the data have been fitted and results output into a MATLAB structure, some analysis must be performed by hand. First, any spectra which MATLAB was unable to successfully fit with the automated procedure must be reviewed manually. This can be done using `view`, as described in Section 4.1.1. Upon inspection, some of these spectra may be discovered to contain corrupted or otherwise useless data and immediately discarded. Others must be fitted individually, perhaps using a different set of starting parameters, for example, an ensemble mean of the successfully fitted spectra.

The final step in reducing the data is to correct the retrieved meridional wind speeds by finding the difference in observations made in 180° pairs (*cf* Equation 2.7), a process carried out by the function `windsdiff`. Minor frequency mis-calibrations can introduced a significant error into velocity determinations. We believe the jumps in the distribution of our raw data, apparent in Figure 4.4, to be due at least in part to calibration issues. However, vertical winds and variations in winds throughout the observed region in may also play a role. Our model, as expressed in Equation 2.7, assumes mesospheric winds to be constant at all points observed. This assumption is least likely to hold for observations at lower elevation which measure emissions from a source region hundreds of km distant.

4.2 General inverse modelling and error analysis

Before turning to the specifics of this study, a brief discussion of the least-squares problem is called for, which will also help to identify and categorize possible sources of uncertainty and error.

First, some definitions: the state vector $\mathbf{a}$ contains the variables to be retrieved, in this case the line's half-width $\Delta\nu$ and Doppler shift ν_{dopp} and an amplitude A. The vector $\mathbf{b}$ contains other parameters on which the measurement depends, which are known exactly by the measurement system, but inexactly by the observer (although some *a priori* knowledge may be available). These include the atmospheric temperature T and f_i, the frequency of each bin. However, we can safely assume the bin frequency to be exact, since the variance Δf_i in bin sensitivity is negligible compared to f_i.

The *forward model* $F(\nu, \mathbf{b})$ consists of the combination of the system under study and the physical measuring system. It is the function that describes way in which the components of the state vector propagate into the measuring apparatus. The *inverse model* $I(\nu, \mathbf{b})$ is the numerical process used to retrieve state parameters from the measured values, which may be defined either algebraically or algorithmically.

The vector of measured valued is $\mathbf{y}$, which in fact is equal to T_A. However, we use $\mathbf{y}$ here for the sake of clarity in nomenclature and to avoid confusion with the atmospheric temperature T).

Let us define the contribution function $\mathbf{D_y}$ to be $\frac{\partial \mathbf{I}}{\partial \mathbf{y}}$. Further, let the weighting functions $\mathbf{K_a}$ and $\mathbf{K_b}$ be the Jacobian matrices defined by $\partial\mathbf{F}/\partial\mathbf{a}$ and $\partial\mathbf{F}/\partial\mathbf{b}$. The retrieved parameters are obtained by mapping $\mathbf{a}$ into y via the forward model and then mapping back via the inverse model.

$$\mathbf{y} = F(\mathbf{a}, \mathbf{b}) + \epsilon_y \quad (4.6)$$

$$\hat{\mathbf{a}} = I(\mathbf{y}, \mathbf{b}) \quad (4.7)$$

The retrieved state $\hat{\mathbf{a}}$ differs from the true state $\mathbf{a}$ by an error $\mathbf{\Delta a}$. These equations can be linearized about some reference value $(\overline{\mathbf{a}}, \overline{\mathbf{b}})$ for the purpose of error analysis:

$$\mathbf{y} = F(\overline{\mathbf{a}}, \overline{\mathbf{b}}) + \mathbf{K_a}(\mathbf{a} - \overline{\mathbf{a}}) + \mathbf{K_b}(\mathbf{b} - \overline{\mathbf{b}}) + \epsilon_y \quad (4.8)$$

$$\mathbf{a} = I(\overline{\mathbf{y}}, \overline{\mathbf{b}}) + \mathbf{D_y}(\mathbf{y} - \overline{\mathbf{y}}) + \mathbf{D_b}(\mathbf{b} - \overline{\mathbf{b}}) \quad (4.9)$$

The reference value could be chosen, for instance, as

the value of the previous iteration, the "true" state, or an ensemble mean (Rodgers, 1990).

If we assume that Gaussian statistics apply for the uncertainties and errors in the measurement and in b, Rodgers (1976) shows that the error in $\mathbf{a}$ is bounded by

$$\mathbf{\Delta a} = \mathbf{D_y}\epsilon_\mathbf{y} + (\mathbf{A}-\mathbf{I})(\mathbf{a}-\overline{\mathbf{a}}) + \mathbf{D_y K_b}(\mathbf{b}-\overline{\mathbf{b}}) \quad (4.10)$$

where $\mathbf{I}$ is the identity matrix.

Equation 4.10 makes clear the nature of the different kinds of uncertainty present in the system:

1. There can be both systematic and random errors that derive from our imperfect knowledge of the physical system. These can include calibration errors, imperfect *a priori* knowledge, and statistical variations in the physical state of the system. Assuming that our theory accurately decribes all the physics of the experiment, the vector $\mathbf{b}$ should be negligible.

2. The second error term in Equation 4.10, known as the null-space error, quantifies the degree of "smoothing" caused by multiplication with the averaging kernel. Its existance derives from "the inherent finite vertical resolution of the observing system" (Rodgers, 1990), or in other words, from the representation of a continuous function by a set of discrete values. For an exact solution, the averaging kernel is equal to the identity matrix. If we choose as our linearization point the value of the previous iteration, the null-space measurement is small.

3. The most significant term, $\mathrm{D}_\mathbf{y}\epsilon_\mathbf{y}$, represents the contribution to the error in $\mathbf{a}$ of uncertainties in the measurement of $\mathbf{y}$. Without forgetting the existance of other sources of uncertainty, we can account for the main source of error in the retrieved parameters by estimating the uncertainties in $\mathbf{y}$ and understanding how that uncertainty propagates into $\mathbf{\Delta a}$.

For iterative least-squares algorithms, $\mathbf{D_y}$ is given by

$$\mathbf{D_y} = \mathbf{S_a K_a^T}(\mathbf{K_a S_a K_a^T} + \mathbf{S}_\epsilon)^{-1}, \quad (4.11)$$

where $\mathbf{S_x}$ and $\mathbf{S}_\epsilon$ are the covariance matrices of x and ϵ_y (Rodgers, 1976) As was mentioned above, it is a reasonable approximation to disregard cross-correlations between frequency bins, i.e., to assume S_ϵ to be a diagonal matrix. The variance in each bin, σ_y, is related to T_{rx}, and can be estimated *a priori*. However, we chose to estimate σ_y using the residuals of our fitted curve:

$$\sigma_y^2 \approx \frac{1}{N-m}\sum_i (F(\hat{\mathbf{a}}, b) - y)^2 \equiv \epsilon_\mathbf{y}^\mathbf{T}\epsilon_\mathbf{y} \quad (4.12)$$

N is the length of the measurement vector, m is the length of the state vector, and $N-m$ is the number of free parameters in the system.

The covariance matrix $\mathbf{S_a}$ can be approximated by using the Jacobian matrix $\mathbf{J}$, output by `lsqcurvefit` after fitting, on the assumption that $\mathbf{J} \approx \mathbf{K_a}$:

$$\mathbf{S_a} \approx [\mathbf{J^T J}]^{-1}\epsilon_y, \quad (4.13)$$

where the inverse function is a matrix inverse. The diagonal elements of $\mathbf{S_a}$ correspond to the squares of the variances in the elements of $\mathbf{a}$.

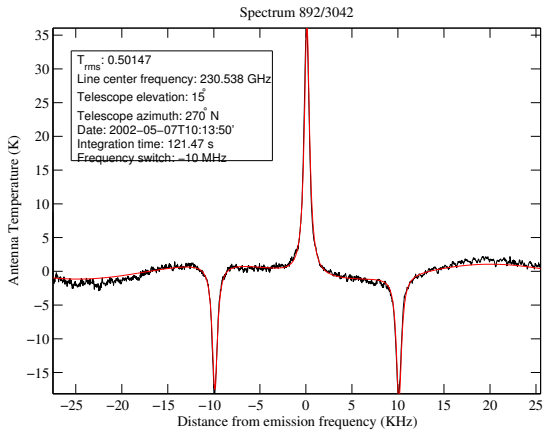

Figure 4.1: Sample folded spectral plot drawn by `view`, with header information and fitted curve displayed on plot.

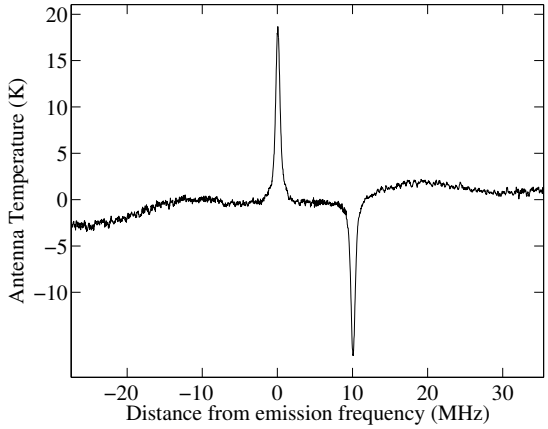

Figure 4.2: Sample raw spectrum, centered on $T_A = 0$, $\nu = \nu_0$.

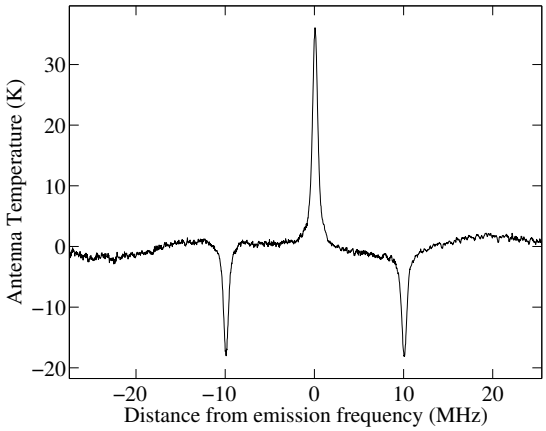

Figure 4.3: Sample spectrum from Figure 4.2, folded by `foldspectrum`.

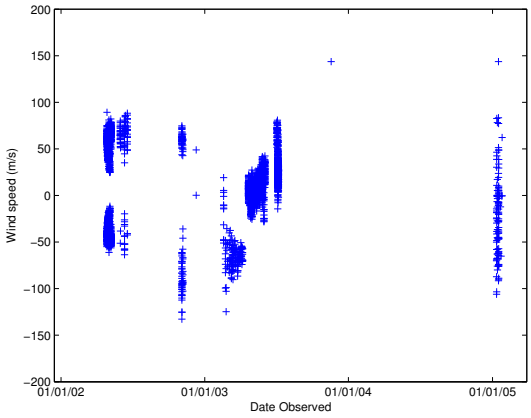

Figure 4.4: Time series of all uncorrected line-of-sight wind speeds output by `timeseriesfo` for the 230 GHz data. We believe the jumps in mean velocity to be caused at least in part by calibration issues with the SIS receiver.

Field name	Description
coffvec	Matrix containing the fitted "coefficient" or state vectors $\mathbf{a}$.
stda	Matrix containing the estimated standard variances in the coefficient vector $\mathbf{a}$.
filevec	Cell containing the names of files included in the series.
time.vec	Vector containing the date as a vector of the format `[YYYY MM DD hh mm ss]`.
time.num	Vector containing the time at which each observation began, as the number of whole and fractional days since Jan 1, 2000.
resnorm	Matrix with rows containing the 2-norm $\frac{1}{2}\|\mathbf{F}(\mathbf{a},\mathbf{x}) - \mathbf{T_b}\|_2^2$ of the residual vector for each spectrum.
residual	Cell containing the residual vectors $\mathbf{F}(\mathbf{a},\mathbf{x}) - \mathbf{T_b}$ for each spectrum.
telaz	Vector containing the telescope's pointing direction in degrees from geographic north (0°).
telalt	Vector containing the telescope's radio pointing elevation in degrees from the surface for each spectrum.
obstime	Vector storing the length of observing time for each spectrum.
velocity	Vector containing the wind speed calculated from the Doppler shift for each spectrum.
$\mathbf{std}_v$	Vector containing the estimated standard variance in the wind speed.

Table 4.1: Summary of the fields in MATLAB structure output by `timeseriesfo`.

Chapter 5

Results and discussion

Frequency-switched observations of mesospheric CO were made periodically between 2002 and 2005, as summarized in Tables 5.2 and 5.1. All spectra were fitted using a least-squares algorithm, as outlined in Chap. 4. Wind speeds were rejected as outliers if they lay more than 2 standard deviations from the mean for the 230 GHz calculations or more than 3.5 standard deviations from the mean for the 461 GHz transitions. Additionally, wind speeds were rejected if their uncertainty was greater than 30 m/s. Because many of the spectra were reduced to uselessness by receiver noise, a large number could not be fitted satisfactorily. Of the 9075 230 GHz measurements, 3534 were rejected due to high residuals between the fitting function and the data. In contrast, of the 5541 fitted spectra, only 14 were rejected as outliers. Fewer of the 460 GHz observations experienced noise problems, so that only 548 high-residual spectra and 7 outliers were rejected out of 2667 spectra. A minority of the rejected spectra appear to contain usable data, and an improved fitting algorithm might allow a handful of other spectra to be processed. However, inspection reveals this to be the exception among the rejected spectra.

In finding the differenced wind speeds, we allowed observations to be combined only if separated by less than 2 hours in time. Hernandez et al. (1995) measured upper mesospheric winds near 87 km altitude using an optical Doppler radar, and determined the dominant oscillations in these winds to have periodicities of 10 h and of greater than 48 h. If the same is true in the lower mesospheric region, the combination of measurements separated by less than 2 h should have little impact on the ability to recognize periodic behavior.

The data displayed in this chapter were taken at a total of 8 equally spaced azimuthal angles. We follow the geographic coordinate system for wind directions, with geographic North equal to 0°, Northeast equal to 45°, and so on. We follow the meterological convention of naming winds based on their direction of origin. In each legend, the direction of wind origin appears first. The figures are consistently color-coded by direction, so that, for instance, a 23 m/s wind out of the south would appear as a green data point (the N-S direction) at -23 m/s.

Figures 5.3, 5.4 and 5.5 summarize the wind speeds derived from CO 461 GHz spectra during July 2003, shortly before mid-winter. Because the carbon monoxide column density is so much greater in winter than in summer, the spectra have a better signal-to-noise ratio and can be fitted more precisely. Both as a whole and individually, these figures seem to be marked by prominent oscillations. Although the data set considered here is too small to make definite claims, an oscillation with a period somewhat greater than 48 h seems apparent upon inspection. It seems plausible that a closer study of these and similar data would reveal the presence of lower-amplitude and higher-frequency waves, including perhaps the 10 h oscillation described by Hernandez et al. (1995).

A surprising feature of the 461 GHz data is the apparent dependence of observed wind speeds on telescope elevation. The wind speeds at 30° elevation, shown in Figure 5.4, are noticeable greater than the corresponding data in Figures 5.3, 5.5, and 5.6.

Date Range		No. of wind determinations	Observed Frequency (GHz)
27 Apr – 18 June	2002	309	230
13 Jan – 16 Jan	2003	17	230
18 Feb – 13 Mar	2003	10	230
3 July – 6 July	2003	17	230
9 July – 17 July	2003	451	461
3 Nov – 6 Nov	2003	22	230
13 Jan – 16 Jan	2005	24	230

Table 5.1: Summary of available data and its distribution in time.

This may be explained by either vertical or horizontal winds that are not uniform throughout the area around the telescope. For example, if the telescope points towards an area of upwelling in the north and an area of downwelling, or even of lesser upwelling in the south, the vertical wind components will not be cancelled by differencing the two line-of-sight velocities.

The only mid-summer AST/RO wind speed data are the results from January 2005 displayed in Figure 5.7. The amplitudes of the measured winds are much greater than the observed winter speeds, evidence of seasonal differences in polar atmospheric transport. In Figure 5.7, the error bars are much larger than in the winter profiles. This can be explained by the much higher CO column density in the winter months, which results in a higher signal-to noise ratio.

[1] These spectra were collected while the telescope was locked into "park" position during inclement weather. These may provide useful data, but cannot be processed by the routine used in this study, as measurements were were not conducted in 180° pairs.

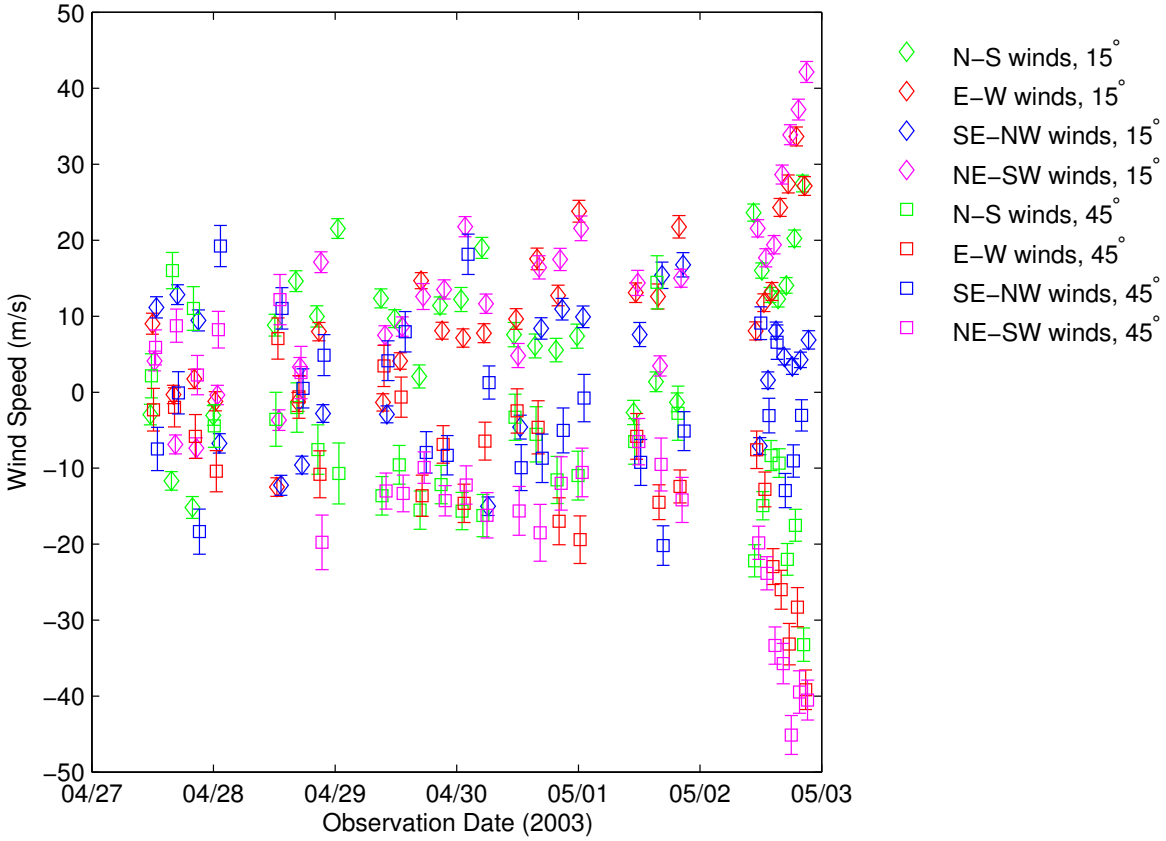

Figure 5.1: These 309 wind speeds were calculated from CO 230 GHz emission lines observed between 27 April and 2 May 2002.

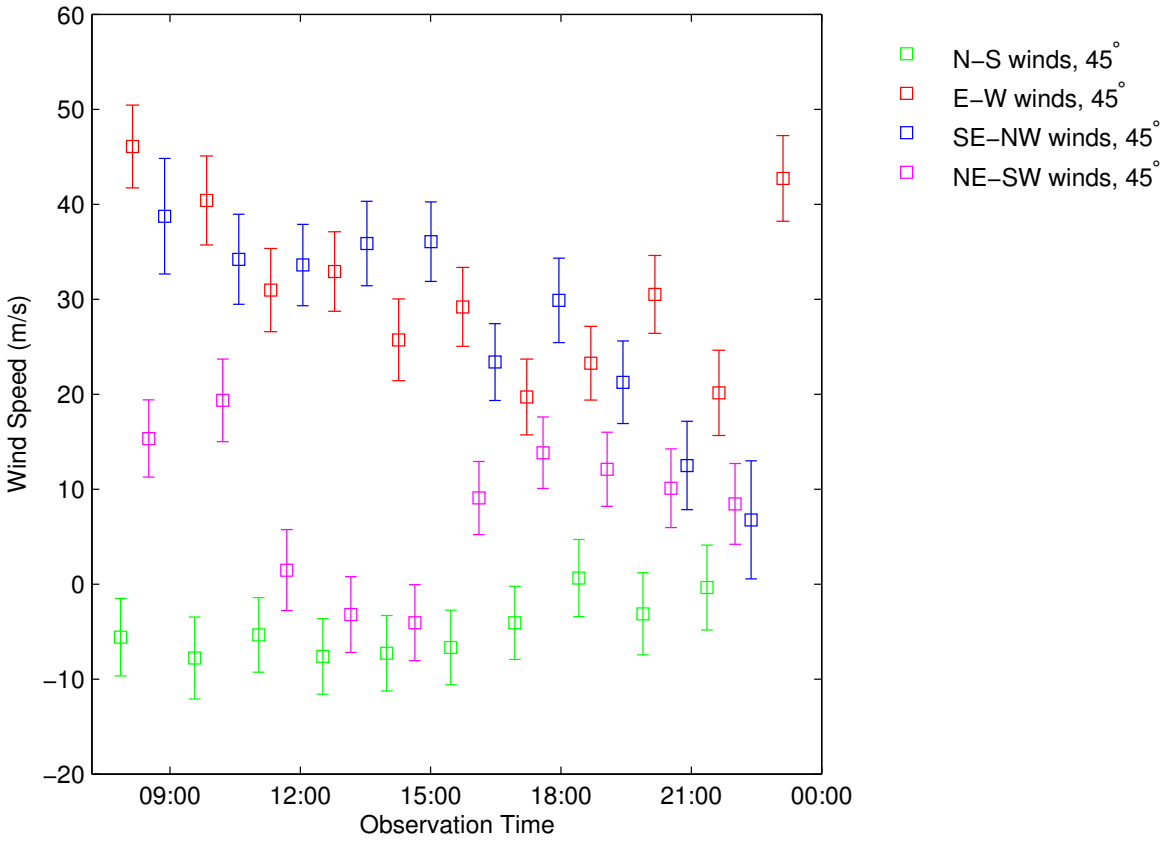

Figure 5.2: Winds speeds retrieved from observations of the CO 230 GHz transition on May 27, 2003.

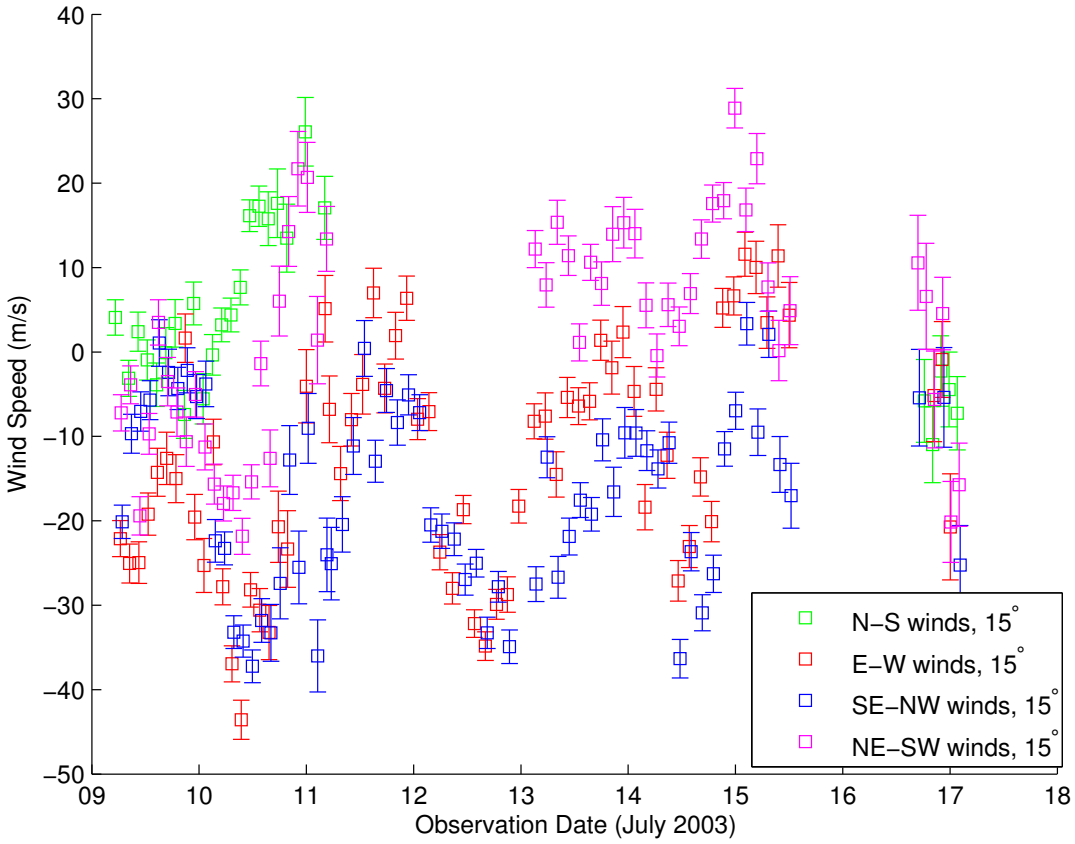

Figure 5.3: All 461 GHz transition measurements taken in July 2003 at a telescope elevation of 15°

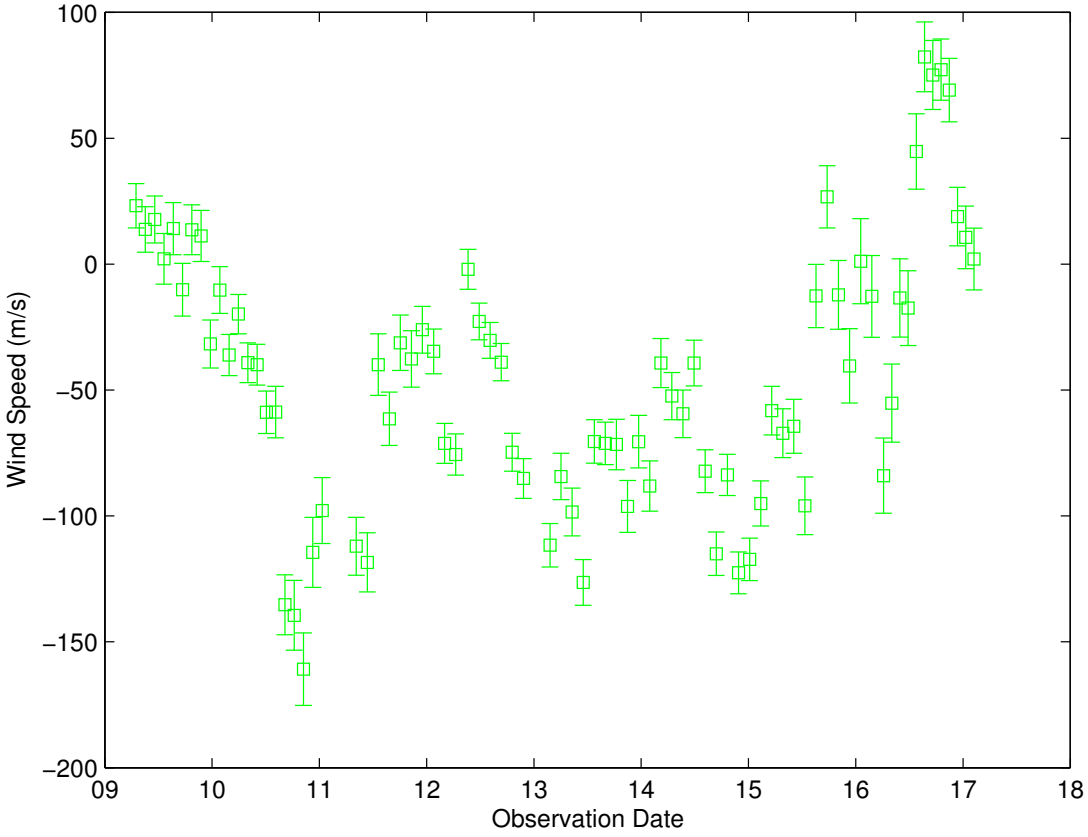

Figure 5.4: All 461 GHz transition measurements taken in July 2003 at a telescope elevation of 30°

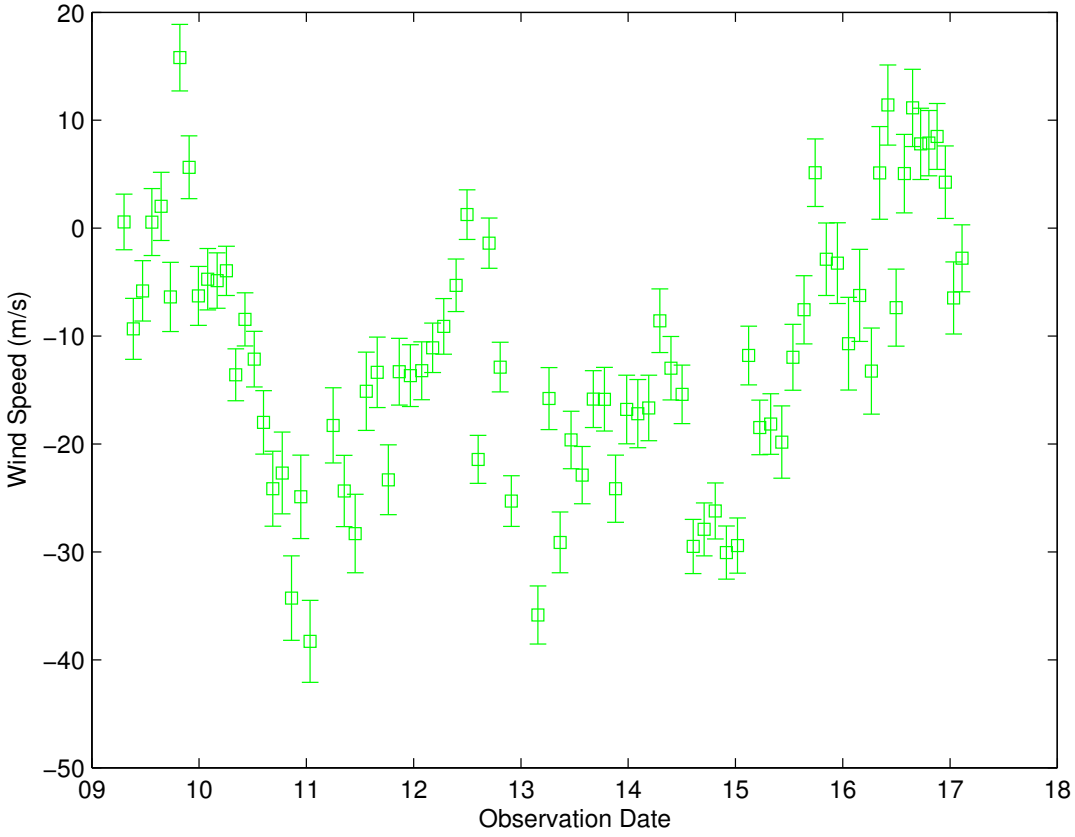

Figure 5.5: All 461 GHz transition measurements taken in July 2003 at a telescope elevation of 45°

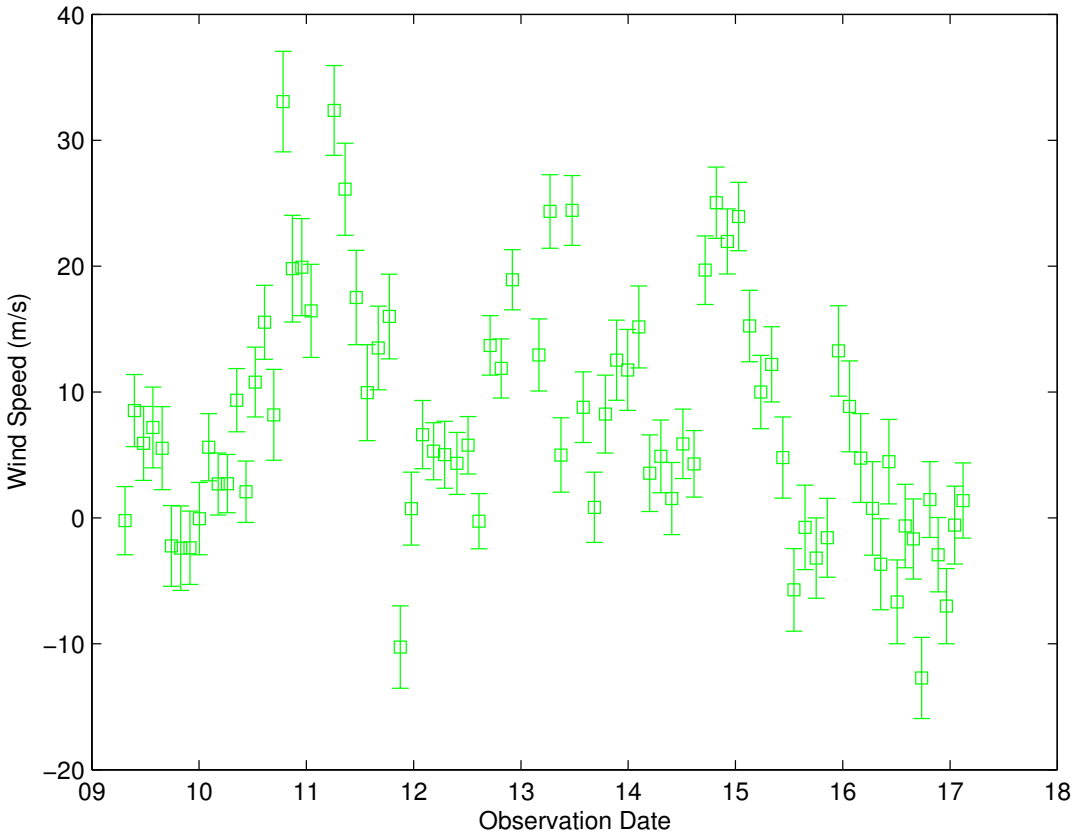

Figure 5.6: All 461 GHz transition measurements taken in July 2003 at a telescope elevation of 65°

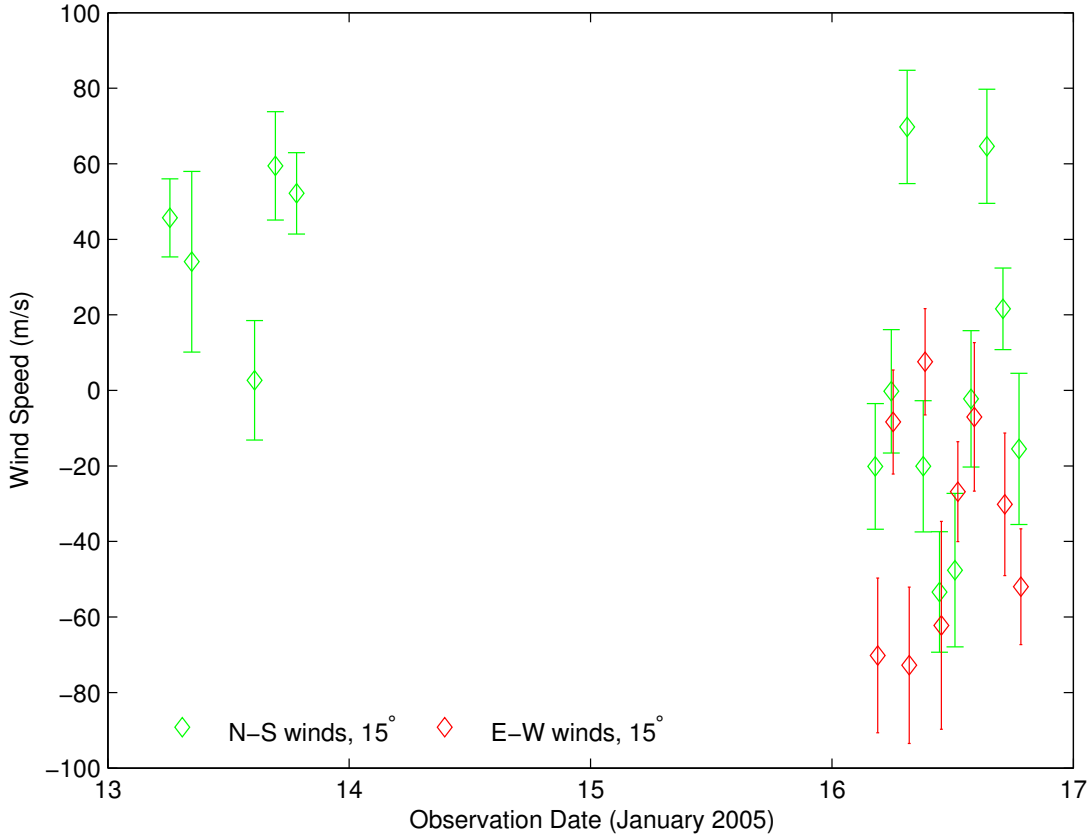

Figure 5.7: Wind speeds derived from 230 GHz transition, January 2005. These are the first mid-summer mesospheric CO profiles collected by AST/RO.

Wavelength observed (GHz)	Rotational transition	Telescope elevation (°)	Number of fitted spectra	Number of wind determinations
230.538	2→1	15	1114	215
		45	1446	326
		75	2963	N/A[1]
461.040	4→3	15	1114	212
		30	323	79
		45	332	80
		65	320	80
		75	23	N/A
Totals			7,635	992

Table 5.2: Summary of mesospheric CO observations made using the AST/RO instrument for the period February 2002 – January 2005.

Chapter 6

Conclusions and Future Directions

A data pipeline was developed for the reduction of atmospheric spectra from the AST/RO telescope. Data from several seasons was analyzed to measure mesospheric advection. Mesospheric wind speeds at the South Pole were found to lie mainly between 0 and 30 m/s, consistent with values measured by Hernandez et al. (1995). A cursory examination of Figures 5.3, 5.4, 5.5 and 5.6 suggest that a larger data set could be used to examine any periodic behavior in polar lower-mesospheric winds.

One weakness of our analysis is the inability to account satisfactorily for the strength or variability of vertical motion in the mesosphere. This may be the cause of the apparently anomalously large wind speeds in Figure 5.4. By more carefully examining the history of the instrument's calibration, we hope to calculate wind speeds for each fitted spectrum individually, without the requirement of a 180 ° counterpart for calibration.

Since fits have been obtained for the full set of CO spectra, estimation of carbon monoxide column densities should be straightforward. Of particular interest is the seasonal dependence of CO concentrations. A marked increase in the intensity of the carbon monoxide emission peak in winter is apparent upon even a cursory examination of the data, but this seasonal contrast has not yet been quantified. Doing so could provide additional confirmation of the theoretical predictions put forward by Garcia & Solomon (1983).

Further work will investigate the vertical profile of both CO concentrations and wind speeds, expanding on the preliminary work by Chamberlin (1997). Resolving an atmospheric vertical profile typically involves fitting a set of "weighting functions" to the data. The weighting functions describe the frequency-dependent reaction of the inverse model to changes in atmospheric parameters. They are chosen so that each function's sensitivity peaks in a narrow altitude range. Several alternative fitting techniques exist for estimation of non-linear functions, including the Twomey-Tikhonov method and the Backus-Gilbert method (*cf.* for instance Janssen, 1993, p. 355; Rodgers, 1976; Rodgers, 1990; Backus & Gilbert, 1967; Bal & Ren, 2005; Press et al., 1992; Bevilacqua & Olivero, 1988). These alternatives may provide better results or a more thourough analysis of model error.

The set of routines developed in this project can be easily expanded or modified for future research involving other spectral lines. Line shapes other than the van Vleck-Weisskopf shape can be investigated simply by substituting a short MATLAB routine describing the form of the new line and its derivative (if possible) for the routine `vvwfo`.

One of the other atmospheric species accessible to the telescope is $^{18}O^{16}O$, which was observed over several days in January 2005. This oxygen isotope is well-mixed throughout the atmosphere. It can serve as a proxy for $O^{16}O^{16}$, which cannot be observed radiometrically because of the breadth of its spectral lines. Because the density profile of $O^{18}O$ is so well known, its spectra can be used to retrieve middle-atmospheric vertical temperature profiles.

Another interesting feature of the $^{18}O^{16}O$ spectrum is that it exhibits Zeeman splitting as a result of the

Earth's geomagnetic field. The magnitude and form of this splitting depends on the orientation of the Earth's magnetic field with respect to the polarisation observed by the telescope. A portion of the observations of the $^{18}O^{16}O$ spectrum were made during an intense geomagnetic storm. In principle, it should be possible to investigate changes in the Earth's geomagnetic field based on the deformations of the line shape over time. The findings could be compared to measurements taken by other instruments, including data gathered by a ground-based magnetometer located at the South Pole as well as aeronomical instruments.

This project has not only produced a set of data on Antarctic mesospheric winds, but has also laid the groundwork for several possible future projects at Oberlin College investigating the Antarctic mesosphere. Future work could be directed towards improving the algorithms used here, investigating periodic oscillations of mesospheric winds, determining the concentrations and vertical profile of mesospheric CO, or studying the effect of a geomagnetic storm on the Antarctic mesosphere. The basic fitting tools developed and the data reduced in this work should prove useful to future students working on any of these related projects.

Bibliography

Allen, D. R., Stanford, J. L., López-Valverde, M. A., Nakamura, N., Lary, D. J., Douglass, A. R., Cerniglia, M. C., Remedios, J. J., & Taylor, F. W. 1999, Journal of Atmospheric Sciences, 56, 563

Allen, D. R., Stanford, J. L., Nakamura, N., López-Valverde, M. A., López-Puertas, M., Taylor, F. W., & Remedios, J. J. 2000, Geophys. Res. Lett., 27, 665

Backus, G. E. & Gilbert, J. F. 1967, Geophysical Journal, 13, 247

Bal, G. & Ren, K. 2005, Inverse Problems, 21, 153

Bevilacqua, R. M. & Olivero, J. J. 1988, J. Geophys. Res., 93, 9463

Brasseur, G. & Solomon, S. 1984, Aeronomy of the middle atmosphere: Chemistry and physics of the stratosphere and mesosphere, Vol. 3 (Dordrecht, D. Reidel Publishing Co.)

Chamberlain, M. A., Ashley, M. C. B., Burton, M. G., Phillips, A., Storey, J. W. V., & Harper, D. A. 2000, The Astrophysical Journal

Chamberlin, R. 2002, in Astronomical Society of the Pacific Conference Series, 172–+

Chamberlin, R. A. 1997, Observation of the Mesospheric Wind Velocity by Detection of Small Doppler Shifts in CO Spectra, Technical Memo 30, AST/RO

Chamberlin, R. A. 2001, J. Geophys. Res., 20101, the radiosonde used here (from 1991-1996) gave anomolously low PWV values, which they try to compensate for by comparison to PWVsat. The calculated dry air opacity is robust.

—. 2004, Publications of the Astronomical Society of Australia, 21, 264

Chamberlin, R. A. & Bally, J. 1994, Appl. Opt., 33, 1095

Chamberlin, R. A., Lane, A. P., & Stark, A. A. 1997, Astrophysical Journal, 476, 428

Clancy, R. T., Muhleman, D. O., & Berge, G. L. 1982, J. Geophys. Res., 87, 5009

Climate Monitoring and Diagnostics Laboratory (CMDL). 2004, CMDL Summary Report, Tech. Rep. 27, U.S. Department of Commerce, National Oceanic and Atmospheric Administration, Environmental Research Laboratories

Committee on Earth Observation Satellites (CEOS). 2003, CEOS Standard Terminology for Microwave Radiometry, This collection of definitions is the product of an ongoing project which aims to compile standard definitions for common terms in the field of microwave rediometry. At the time of writing, Chapters I and II of the document were available at: *http://www.boulder.nist.gov/div813/stdterms/CEOS“˙Ch12“˙current.pdf*

de Zafra, R. L. & Muscari, G. 2004, Journal of Geophysical Research (Atmospheres), 109, 6105

Forbes, J. M., Portnyagin, I. Y., Makarov, N. A., Palo, S. E., Merzlyakov, E. G., & Zhang, X. 1999, Earth, Planets, and Space, 51, 611

Fukushima, N. 1995, I.U.G.G. Chronicle, 226, 73

Garcia, R. R. & Solomon, S. 1983, J. Geophys. Res., 88, 1379

Hedin, A. E. 1987, J. Geophys. Res., 92, 4649

Hernandez, G. 1999, J. Geophys. Res., 104, 10355

Hernandez, G., Forbes, J. M., Smith, R. W., Portnyagin, Y., Booth, J. F., & Makarov, N. 1996, Geophys. Res. Letters, 23, 1079

Hernandez, G., Smith, R. W., & Conner, J. F. 1992, Geophys. Res. Lett., 19, 53

Hernandez, G., Smith, R. W., & Fraser, J. G. 1995, Advances in Space Research, 16, (5)71

Houghton, J. T., Ding, Y., Griggs, D. J., Noguer, M., van der Linden, P. J., x. Dai, Maskell, K., & Johnson, C. A., eds. 2001, Climate Change 2001: The Scientific Basis: Contribution of Working Group I to the Third Assessment Report of the Intergovernmental Panel on Climate Change (New York: Cambridge University Press)

Houghton, J. T. & et al., eds. 1996, Climate Change 1995 : the Science of Climate Change (Report of the International Panel on Climate Change)

Huang, M. 2001, PhD thesis, Boston University

Ingalls, J. G. 1999, PhD thesis, Boston University

Janssen, M. A., ed. 1993, Atmospheric Remote Sensing by Microwave Radiometry, Wiley Series in Remote Sensing (John Wiley & Sons, Inc.)

Labitzke, K., Barnett, J. J., & Edwards, B., eds. 1985, Handbook MAP 16 (SCOSTEP, University of Illinois, Urbana)

Levenberg, K. 1944, Quarterly Applied Math, 2, 164

Lübken, F., Jarvis, M. J., & Jones, G. O. L. 1999, Geophys. Res. Lett., 26, 3581

Marquardt, D. 1963, SIAM Journal Applied Math

Marsh, S. H., Bennett, R. G. T., Baggaley, W. J., Fraser, G. J., & Plank, G. E. 2000, J. Atmos. Solar-Terr. Phys., 62, 1129

Pan, W. & Gardner, C. S. 2003, J. Geophys. Res., 108, 4564

Pardo, J. R., Cernicharo, J., & Serabyn, E. 2001, IEEE Transactions on Antennas and Propagation, 49, 1683

Pickett, H. M., Poynter, R. L., Cohen, E. A., Delitsky, M. L., Pearson, J. C., & Muller, H. S. P. 1998, J. Quant. Spectrosc. & Rad. Transfer, 60, 883

Portnyagin, Y. I., Forbes, J. M., & Makarov, N. A. 1997, Geophys. Res. Lett., 24, 81

Portnyagin, Y. I., Forbes, J. M., Merzlyakov, E. G., Makarov, N. A., & Palo, S. E. 2000, Annales Geophysicae, 18, 547

Press, W. H., Teukolsky, S. A., Vetterling, W. T., & Flannery, B. P. 1992, Numerical recipes in FORTRAN. The art of scientific computing (Cambridge: University Press, —c1992, 2nd ed.)

Rodgers, C. D. 1976, Reviews of Geophysics and Space Physics, 14, 609

Rodgers, C. D. 1990, J. Geophys. Res., 95, 5587

Schieder, R., Tolls, V., & Winnewisser, G. 1989, Experimental Astronomy, 1, 101

Solomon, S., Garcia, R. R., Olivero, J. J., Bevilacqua, R. M., Schwartz, P. R., Clancy, R. T., & Muhleman, D. O. 1985, Journal of Atmospheric Sciences, 42, 1072

Stark, A. A., Bally, J., Balm, S. P., Bania, T. M., Bolatto, A. D., Chamberlin, R. A., Engargiola, G., Huang, M., Ingalls, J. G., Jacobs, K., Jackson, J. M., Kooi, J. W., Lane, A. P., Lo, K.-Y., Marks, R. D., Martin, C. L., Mumma, D., Ojha, R., Schieder, R., Staguhn, J., Stutzki, J., Walker, C. K., Wilson, R. W., Wright, G. A., Zhang, X., Zimmermann, P., & Zimmermann, R. 2001, Publ. Astron. Soc. Pac., 113, 567

Stark, A. A., Chamberlin, R. A., Ingalls, J. G., Cheng, J., & Wright, G. 1997, Review of Scientific Instruments, 68, 2200

Townes, C. H. & Schawlow, A. 1975, Microwave Spectroscopy (Dover Publications, Inc.)

van Vleck, J. H. & Weisskopf, V. F. 1945, Reviews of Modern Physics, 17, 227

Waters, J. W., Wilson, W. J., & Shimabukoru, F. I. 1976, Science, 191, 1171

Wattenbach, R., Durwen, E. J., Röser, H. P., & Schultz, G. V. 1984, J. Geophys. Res.-Atmos., 89, 7285